PAPER

Three-dimensional plasma edge turbulence simulations of the Mega Ampere Spherical Tokamak and comparison with experimental measurements

IOP Publishing Plasma Physics and Controlled Fusion
Plasma Phys. Control. Fusion **61** (2019) 095013 (19pp) https://doi.org/10.1088/1361-6587/ab3561

Three-dimensional plasma edge turbulence simulations of the Mega Ampere Spherical Tokamak and comparison with experimental measurements

Fabio Riva[1], Fulvio Militello[1], Sarah Elmore[1], John T Omotani[1], Ben Dudson[2], Nick R Walkden[1] and the MAST team

[1] United Kingdom Atomic Energy Authority, Culham Centre for Fusion Energy, Culham Science Centre, Abingdon, Oxon, OX14 3DB, United Kingdom
[2] York Plasma Institute, Department of Physics, University of York, Heslington, York YO10 5DQ, United Kingdom

E-mail: fabio.riva@ukaea.uk

Received 27 March 2019, revised 17 June 2019
Accepted for publication 22 July 2019
Published 13 August 2019

Abstract

The STORM module of BOUT++ (Easy *et al* 2014 *Phys. Plasmas* **21** 122515) is generalized to simulate plasma turbulence at the periphery of tokamak devices in diverted configurations and it is used to carry out three-dimensional nonlinear flux-driven simulations in double null configuration with realistic experimental parameters of an L-mode plasma discharge in the Mega Ampere Spherical Tokamak. The reliability of STORM in modeling the scrape-off layer (SOL) plasma dynamics is assessed by comparing the numerical results with experimental measurements from a reciprocating Gundestrup probe and from flush-mounted Langmuir probes. This is the first time that a thorough comparison between experimental measurements and three-dimensional simulations in double null configuration is attempted. It is found that the simulations correctly capture most of the statistical properties of plasma turbulence at the outer mid-plane, whereas ion saturation current and floating potential time-averaged profiles at the outer mid-plane are steeper in the simulations than in the experiment. In particular, it is found that the ion saturation current and floating potential probability distribution functions, as well as the power spectra and several statistical properties of intermittent events in the tokamak SOL, such as the shape, duration and separation of burst events are correctly described by the STORM model. Good qualitative agreement is also obtained for the time-averaged ion saturation current density profiles at the divertor plates. On the other hand, the ion saturation current decay length is approximately 4 times smaller in the numerical results than in the experimental measurements. Additionally, the level of the fluctuations is smaller in the simulations than in the experiment. Finally, possible areas of improvement for the STORM model are identified.

Keywords: turbulence, validation, scrape-off layer

(Some figures may appear in colour only in the online journal)

1. Introduction

Understanding the phenomena at play in the tokamak scrape-off layer (SOL) is a crucial challenge for ITER and future fusion devices [1]. The SOL regulates the exhaust of heat and particles at the divertor plates and at the first wall, which must be designed to sustain high thermal loads that are at the edge or above current material limits [2]. It is therefore essential to improve our ability to model the transport mechanisms governing the SOL plasma dynamics. Reaching predictive

capabilities for the heat and particle loads on tokamak plasma-facing components is extremely challenging, since complex nonlinear turbulent plasma phenomena on a wide range of spatio-temporal scales are involved in the SOL region. In addition, the cross-field transport is characterized by large intermittent events, the so-called filaments. The problem is further complicated by the complex magnetic geometry involved at the periphery of tokamak devices and by the presence of plasma sheaths at the divertor targets. As a consequence, state-of-the-art simulation codes based on first-principles models are required to uncover the SOL plasma physics [3, 4].

In the past years, a number of two- and three-dimensional fluid turbulence codes have been developed to study the plasma dynamics at the periphery of tokamak devices, such as the Hermes [5] and the STORM [6, 7] modules of BOUT++ [8, 9], ESEL [10, 11] and its hot ion counterpart HESEL [12], and GBS [13, 14], GDB [15], GRILLIX [16], and TOKAM3X [17]. All the mentioned codes are based on a set of drift-reduced Braginskii equations [18, 19], but they differ in their assumptions to simplify the equations and in their numerical algorithms. During the past years, these codes have provided interesting insight into the dynamics of SOL plasmas, for example by improving our understanding of the relation between line-averaged density and broadening of SOL radial profiles [20], of the dependence in limited configuration of the SOL width on plasma parameters [21, 22], and of the spreading of plasma turbulence into the private flux region (PFR) [23].

To increase the reliability of the results of such codes, in the past few years the fusion community dedicated specific projects to develop and apply verification and validation procedures [24–26]. In particular, a methodology based on the method of manufactured solutions was ported to the fusion community [27], and it is now routinely used for verifying plasma simulation codes (see, e.g. [16, 17, 28]). Moreover, simulations of isolated filaments were validated against experimental measurements from basic plasma physics experiments [29] and tokamak devices [30], shedding light on the mechanisms that set the dynamics of these structures. Plasma turbulence simulations were also validated against measurements obtained from basic plasma physics experiments and tokamak devices, improving our understanding of the phenomena that govern the cross-field transport in these experiments (see, e.g. [31–34]). Despite this progress, several crucial issues remain open, in particular for diverted configurations (fusion reactor will be diverted).

In this paper, we report on a comparison between an L-mode Mega Ampere Spherical Tokamak (MAST) plasma discharge and a number of three-dimensional fluid turbulence simulations carried out with STORM. More precisely, we perform simulations in disconnected lower double null configuration of the MAST plasma discharge #21712 and we compare the numerical results with measurements from a Gundestrup probe installed on a reciprocating manipulator at the outer mid-plane and from flush-mounted Langmuir probes (LPs) at the outer divertor plates. The impact of collisional dissipation parameters on the numerical results is also studied.

The goal of the present investigation is threefold. First, we present for the first time three-dimensional plasma turbulence simulations carried out with STORM in double null tokamak geometry with realistic plasma conditions. This represents a major step in the development of STORM, since most of the simulations performed in the past with this code were obtained considering simplified geometries or isolated filaments (see, e.g. [6, 23, 35–37]). Second, we extend the work presented in [33] by relaxing some of the assumptions used in that study. In particular, we account for three-dimensional effects and for parallel currents to the divertor plates, shedding light on their impact on the SOL plasma dynamics. Third, we perform a validation of the STORM model against experimental measurements. This allows assessing the maturity of the STORM model in describing the mechanisms that govern the SOL transport and to identify possible areas of improvement for the model.

The present paper is structured as follows. After this introduction, in sections 2 and 3 we discuss the experimental setup and the physical model considered for our investigation, respectively. Then, in section 4 we present the STORM simulations of the MAST plasma discharge #21712. In sections 5 and 6 the numerical results are compared with experimental measurements from a reciprocating probe at the tokamak outer mid-plane and from flush-mounted LPs at the divertor targets, respectively. Finally, we report our conclusions in section 7. The boundary conditions considered in our study, the investigation of the impact of grid resolution on simulation results, and the discussion of obtaining synthetic ion saturation current and floating potential time traces from STORM simulations are the subjects of appendixes A, B, and C, respectively.

2. Experimental setup

The MAST experiment was a low aspect ratio spherical tokamak with major and minor radii $R = 0.85\,\mathrm{m}$ and $a = 0.59\,\mathrm{m}$, respectively. MAST was well equipped with diagnostics for edge studies, including a fast reciprocating probe system [38] equipped with a Gundestrup probe [39] and arrays of high spatial and temporal resolution LPs covering all four targets [40]. For this reason, MAST was an ideal test bed for validating the STORM model against experimental measurements.

In the present work we focus on the ohmic L-mode pulse #21712, which was a deuterium plasma discharge in disconnected lower double null configuration. This discharge was characterized by a plasma current $I_p = 400\,\mathrm{kA}$ and a toroidal magnetic field on axis $B_T \simeq 0.4\,\mathrm{T}$, corresponding to $q_{95} \approx 6.2$. During the flat-top phase the core electron temperature was $T^{\mathrm{core}} \approx 650\,\mathrm{eV}$ and the line-averaged density was $\bar{n} \approx 1.7 \cdot 10^{19}\,\mathrm{m}^{-3}$. Moreover, this pulse was characterized at the last closed flux surface (LCFS) by the reference edge quantities shown in table 1. We refer to [41] for more details on the experimental investigation of this plasma discharge.

The experimental measurements presented in the following were obtained during the flat-top phase, between $t = 0.2\,\mathrm{s}$ and $t = 0.4\,\mathrm{s}$, with the mid-plane reciprocating Gundestrup probe and with the LPs at the outer divertor targets. The Gundestrup probe reciprocates in the plasma,

Table 1. Reference plasma density n_0, electron and ion temperatures T_{e0} and T_{i0} [33], and magnetic field amplitude $B_0 = \sqrt{B_{\varphi 0}^2 + B_{p0}^2}$ (B_φ and B_p are the toroidal and poloidal magnetic field components), evaluated at the outer mid-plane of the LCFS for the MAST discharge #21712.

n_0 [10^{-19} m^{-3}]	T_{e0} [eV]	T_{i0} [eV]	B_0 [T]
0.5	15	30	0.3

reaching its deepest position at approximately 4 cm inside the separatrix. The probe head is equipped with eight pins (1–8), uniformly distributed at the end of a boron nitride cylinder and biased to −200 V, measuring the ion saturation current, $I_{\rm sat}$, and with 3 additional pins (9–11), located at the front of the probe, used to measure the floating potential, $V_{\rm fl}$. All 11 pins acquired data at 500 kHz. In the following, we refer to pins 1 and 9 for $I_{\rm sat}$ and $V_{\rm fl}$ measurements, respectively (we note that this choice does not affect the conclusions presented in the following of the present paper, since similar results would be obtained with the other pins). A more detailed description of the Gundestrup probe used for this investigation is given in [41]. The flush-mounted LPs were used in swept mode to obtain the *I*–*V* characteristics at the target plates and reconstruct the time-averaged ion saturation current density $\langle j_{\rm sat}\rangle_t$, where $\langle - \rangle_t$ denotes averaging over time.

Since the plasma parameters remained approximately constant and equal to the nominal values given above between $t = 0.2$ s and $t = 0.4$ s, the outer mid-plane plasma quantities discussed in the following are obtained by splitting the $I_{\rm sat}$ and $V_{\rm fl}$ Gundestrup probe signals in a number of sub-signals of 2 ms and considering each sub-signal as an independent measurement at constant radial location (note that we use only measurements from the reciprocating manipulator entering the plasma). This time window is chosen short enough such that the radial displacement of the probe during each sub-interval is small ($\ll$1 cm), but long enough to contain several typical turbulent time scales. We note that $V_{\rm fl}$ signals are processed with a low-pass filter at 125 kHz. We also note that, during MAST discharges, the strike points were naturally sweeping at the targets due to the fringing field from the tokamak solenoid that was not compensated. Therefore, the $\langle j_{\rm sat}\rangle_t$ profiles obtained with the flush-mounted LPs are computed by splitting the raw probe signals in intervals of 1 ms and reconstructing the *I*–*V* characteristic on each resulting sub-interval. Radial profiles are then obtained by averaging together the results from four subsequent sub-intervals. Finally, we note that the position of the separatrix is reconstructed with EFIT [42]. Standard uncertainties in the magnetic reconstruction of the equilibrium imply that the radial location of the measurements with respect to the separatrix is known with a precision of approximately 1 cm. Therefore, the experimental measurements presented in the following are shifted in the radial direction, within this uncertainty, to approximately match the maximum of the time-averaged $V_{\rm fl}$ and $j_{\rm sat}$ numerical profiles at the outer mid-plane and at the divertor plates, respectively (note that a similar approach is discussed in [43]).

3. STORM physical model

Due to the high plasma collisionality typical of the tokamak SOL in L-mode, medium-size devices, the STORM model is based on a set of electrostatic drift-reduced Braginskii equations [6, 7, 18, 19] (we note that the electron collisionality for the plasma discharge #21712 is $\nu_e^* \equiv L_\parallel/\lambda_e \approx 20$ [33], being $L_\parallel$ the mid-plane to target connection length and λ_e the electron mean free path). Additionally, the cold-ion and Boussinesq approximations are employed to simplify the equations (a discussion of using the Boussinesq approximation in modeling the SOL plasma dynamics is found in [44–47]). The resulting system of equations corresponds to an extension of the one used in [7] with the inclusion of metric terms accounting for the realistic three-dimensional axisymmetric magnetic geometry.

Our physical model is written in Bohm normalized units as:

$$\frac{{\rm d}n}{{\rm d}t} = -\nabla\cdot(nV\mathbf{b}) + C(p) - nC(\phi) + \mu_{n0}\nabla_\perp^2 n + S_n, \tag{1}$$

$$\frac{{\rm d}\Omega}{{\rm d}t} = -U\partial_\parallel\Omega + \frac{1}{n}\nabla\cdot(J_\parallel\mathbf{b}) + \frac{C(p)}{n} + \mu_{\Omega 0}\nabla_\perp^2\Omega, \tag{2}$$

$$\frac{{\rm d}U}{{\rm d}t} = -U\partial_\parallel U - \partial_\parallel\phi - \eta_\parallel J_\parallel + 0.71\partial_\parallel T + \mu_{U0}\nabla_\perp^2 U - \frac{US_n}{n}, \tag{3}$$

$$\frac{{\rm d}V}{{\rm d}t} = -V\partial_\parallel V + \frac{m_i}{m_e}\left(\partial_\parallel\phi + \eta_\parallel J_\parallel - \frac{\partial_\parallel p}{n} - 0.71\partial_\parallel T\right) + \mu_{V0}\nabla_\perp^2 V - \frac{VS_n}{n}, \tag{4}$$

$$\begin{aligned}\frac{3}{2}n\frac{{\rm d}T}{{\rm d}t} = &-\frac{3}{2}nV\partial_\parallel T - \nabla\cdot(q_\parallel\mathbf{b}) - 0.71J_\parallel\partial_\parallel T \\ &- p\nabla\cdot(V\mathbf{b}) + TC(p) + \frac{5}{2}pC(T) - pC(\phi) \\ &+ \frac{m_e}{m_i}\frac{V^2}{2}C(p) + \eta_\parallel J_\parallel^2 + \mu_{T0}\nabla_\perp^2 T + S_E \\ &+ \frac{m_e}{m_i}\frac{V^2}{2}S_n - \frac{3}{2}TS_n,\end{aligned} \tag{5}$$

where ϕ is the plasma potential, U and V the parallel (to the magnetic field $\mathbf{B}$) ion and electron velocities, $\Omega = \nabla\cdot(B^{-2}\nabla_\perp\phi)$ the scalar vorticity, $J_\parallel = n(U - V)$ the parallel current, $p = nT$ the electron pressure, $q_\parallel = -\kappa_{\parallel 0}T^{5/2}\partial_\parallel T - 0.71TJ_\parallel$ the parallel electron heat flux, and m_i/m_e the ion to electron mass ratio. In addition, ${\rm d}f/{\rm d}t = \partial f/\partial t + [\phi, f]$, $[\phi, f] = \mathbf{b}\times\nabla\phi\cdot\nabla f$, $\partial_\parallel f = \mathbf{b}\cdot\nabla f$, $C(f) = \nabla\times(\mathbf{b}/B)\cdot\nabla f$, $\nabla_\perp f = \nabla f - \mathbf{b}\partial_\parallel f$, $\nabla_\perp^2 f = \nabla\cdot\nabla_\perp f$, with f a three-dimensional scalar field, B the norm of the magnetic field and $\mathbf{b}$ the unit vector parallel to $\mathbf{B}$. Collisional coefficients are the normalized resistivity

$$\eta_\parallel = 0.51\frac{\nu_{ei0}}{T^{3/2}\Omega_{e0}}, \tag{6}$$

the normalized parallel heat conductivity

$$\kappa_{\parallel 0} = 3.16\frac{T_{e0}}{\nu_{ei0} m_e c_{s0} \rho_{s0}}, \tag{7}$$

and the normalized classical particle diffusivity, viscosity, and perpendicular electron heat conductivity

$$\mu_{n0} = (1 + T_{i0}/T_{e0})\frac{\rho_{e0}^2 \nu_{ei0}}{\rho_{s0}^2 \Omega_{i0}}, \qquad \mu_{\Omega 0} = \frac{3}{4}\frac{\rho_{i0}^2 \nu_{ii0}}{\rho_{s0}^2 \Omega_{i0}},$$
$$\mu_{T0} = 4.66\frac{\rho_{e0}^2 \nu_{ei0}}{\rho_{s0}^2 \Omega_{i0}}, \tag{8}$$

respectively, where the reference ion, electron and ion sound gyro-radii ρ_{i0}, ρ_{e0}, and ρ_{s0}, ion and electron gyro-frequencies Ω_{i0} and Ω_{e0}, ion–ion and ion–electron collision frequencies ν_{ii0} and ν_{ei0}, and ion sound speed c_{s0} are calculated with the reference ion and electron temperatures T_{i0} and T_{e0}, magnetic field B_0, and density n_0. We note that, while we retain the dependence on n and T in computing $q_\parallel$ and $\eta_\parallel$, the classical particle diffusivity, viscosity, and perpendicular electron heat conductivity are assumed homogeneous and constant across the domain. We also note that finite ion temperature corrections are retained in computing μ_{n0} and $\mu_{\Omega 0}$. The coefficients μ_{U0} and μ_{V0} are introduced to guarantee numerical stability. Moreover, the plasma and energy sources S_n and S_E are used to mimic the generation of plasma particles because of ionization and the heat outflowing from the core. Finally, we note that the standard Bohm's normalization is employed in this section (for its definition see, e.g. [7]).

Equations (1)–(5) are completed by a set of boundary conditions describing the plasma dynamics at the magnetic pre-sheath entrance, where the drift-approximation breaks down. More precisely, at the targets we impose Bohm's sheath boundary conditions for the parallel velocities U and V and we compute the parallel electron power flux, $Q_\parallel$, according to [48]. Therefore, at the divertor targets we require

$$U|_{\text{target}} \geqslant \sqrt{T},$$
$$V|_{\text{target}} = \begin{cases} \sqrt{T}\exp\left(\Lambda - \dfrac{\phi}{T}\right) & \text{if } \phi > 0 \\ \sqrt{T}\exp(\Lambda) & \text{otherwise} \end{cases},$$
$$Q_\parallel|_{\text{target}} = \gamma n T V, \tag{9}$$

if $\mathbf{B}$ is directed towards the wall, while we reverse the signs otherwise. Here $\Lambda = -0.5\ln(2\pi m_e/m_i)$ is Bohm's sheath potential and $\gamma = 2 + \Lambda$. The boundary condition for the parallel electron heat flux is then obtained as

$$q_\parallel|_{\text{target}} = Q_\parallel - \frac{5}{2} n T V - 0.5\frac{m_e}{m_i} n V^3. \tag{10}$$

A field-aligned coordinate system (x, y, z) is employed to express equations (1)–(5), where $x = \psi - \psi_0$ is a flux-surface coordinate, $y = \theta$ a parallel coordinate, and $z = \varphi - \int_0^\theta \nu(\psi, \theta')\mathrm{d}\theta'$ a field-line label, with (ψ, θ, φ) an orthogonal toroidal coordinate system, ψ_0 the poloidal flux on axis, φ the toroidal angle, θ a poloidal angle that satisfies $\nabla\theta \cdot \nabla\psi = \nabla\theta \cdot \nabla\varphi = 0$, and $\nu(\psi, \theta) = \mathbf{B} \cdot \nabla\varphi/(\mathbf{B} \cdot \nabla\theta)$ the local field-line pitch. Note that here $\mathbf{B} \cdot \nabla x = \mathbf{B} \cdot \nabla z = 0$ and we assume an axisymmetric geometry. A twist-shift boundary condition [49] is applied in the core to ensure periodicity of field values. Moreover, to guarantee continuity of radial derivatives, these are expressed in quasi-ballooning coordinates [50]. Finally, assuming $k_\perp \gg k_\parallel$, the differential operators $[\phi, -]$, $\nabla_\perp^2(-)$, and $\nabla_\perp(-)$ are simplified by neglecting y (parallel) derivatives. We refer to [8] for more details on the coordinate system used in BOUT++.

4. Numerical setup

To perform three-dimensional plasma turbulence simulations in MAST realistic geometry, we implemented in STORM the modifications discussed in section 3. All x and y derivatives in equations (1)–(5) are computed using second order centered finite difference schemes, except for the Poisson's brackets, which are discretized with a second order Arakawa scheme [51], and the advection terms $U\partial_\parallel(-)$ and $V\partial_\parallel(-)$, which are discretized with second order upwind schemes. Additionally, we exploit periodicity in φ to perform z derivatives in Fourier space. The Poisson's equation $\Omega = \nabla \cdot (B^{-2}\nabla_\perp\phi)$ is therefore inverted in the x–z plane by solving for each Fourier mode a tridiagonal system of equations with the Thomas algorithm [52] (y derivatives are neglected for this, as mentioned in section 3). Moreover, assuming that plasma turbulence in the SOL is characterized by large toroidal mode numbers $n \gg 1$, first order z derivatives are neglected with respect to second order z derivatives in solving the Poisson's equation (this approach is adopted for numerical stability reasons). Time integration is performed adopting the Method of Lines approach and using the CVODE implicit time integration solver from the SUNDIALS suite [53]. Furthermore, we note that, to avoid grid-scale oscillations, U, V, and $q_\parallel$ are solved on a grid staggered by half a point in y and fourth-order interpolation schemes are used to interpolate field quantities from the collocated grid to the staggered grid and vice versa. We refer to [8, 9] for more details on the numerical algorithms implemented in BOUT++ (note that BOUT++ v3.1 is used for the present investigation).

Focusing on the MAST discharge #21712 discussed in section 2, the dissipation coefficients, which are given as input to STORM, are calculated according to equations (6)–(8) with the reference parameters given in table 1. The results are presented in the first row of table 2. However, to increase the numerical stability of STORM simulations, for our reference case in the following we consider $\mu_{n0} = \mu_{T0} = \mu_{U0} = \mu_{V0} = 0.001$ (as also reported on the second row of table 2, referred to as 'Reference' simulation). The impact of collisional parameters on the results of plasma turbulence simulations is investigated in sections 5 and 6 by considering three additional simulations with (i) increased normalized resistivity $\eta_\parallel T^{3/2} = 1.4 \cdot 10^{-4}$(this corresponds to approximately an increase by a factor 5), in the following referred to as 'High $\eta_\parallel$'; (ii) increased viscosity $\mu_{\Omega 0} = 0.008$ (this corresponds to approximately an increase by a factor 6), in the following referred to as 'High $\mu_{\Omega 0}$'; and (iii) $\mu_{n0} = \mu_{T0} = \mu_{U0} = \mu_{V0} = 2.5 \cdot 10^{-4}$, in the following referred

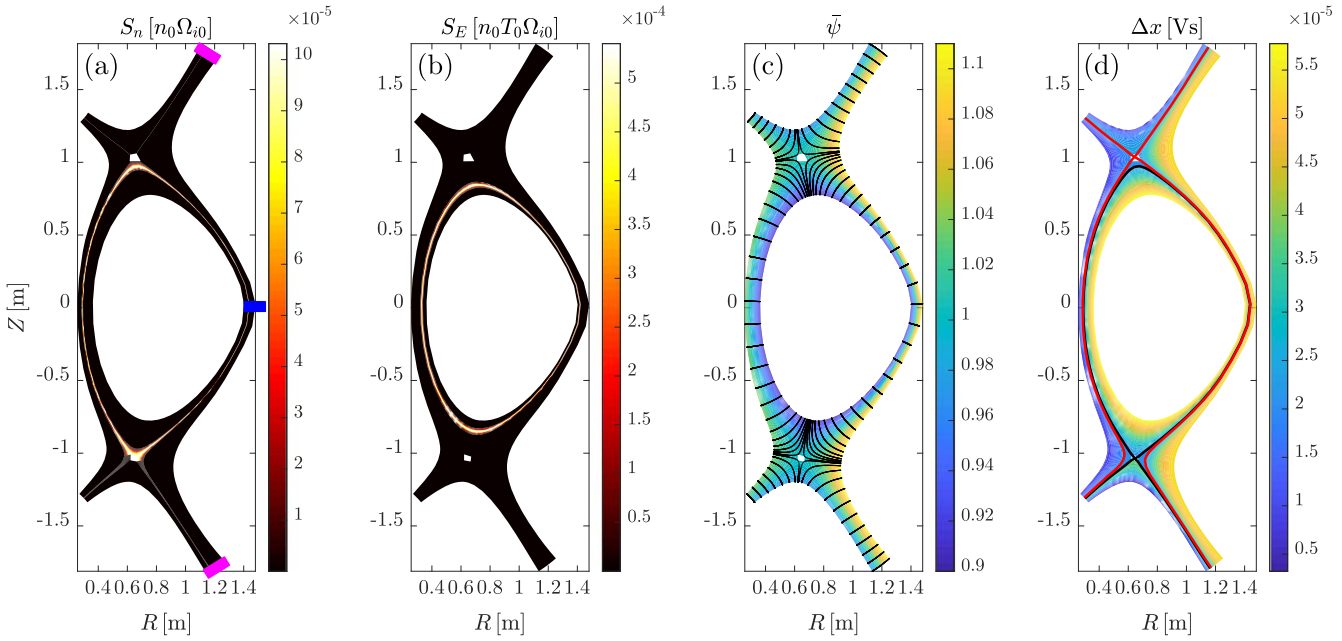

Figure 1. Poloidal cross sections of (a) the particle source S_n; (b) the energy source S_E; (c) the normalized poloidal flux $\bar{\psi}$, with black lines denoting the planes of constant y used in the simulations; and (d) the radial grid spacing Δx, with black and red lines denoting the inner and outer separatrices, respectively (these are separated by approximately 6 mm at the outer mid-plane). The blue and pink rectangles on panel (a) denote approximately the position of the reciprocating probe and of the LPs, respectively, as discussed in section 2.

Table 2. Normalized collisional dissipation coefficients for the MAST discharge #21712 computed according to equations (6)–(8), and as used in the 'Reference', 'High $\eta_\parallel$', 'High $\mu_{\Omega 0}$', and 'Low $\perp$ dissipation' simulations.

Case	$\eta_\parallel T^{3/2}$	$\kappa_{\parallel 0}$	μ_{n0}	$\mu_{\Omega 0}$	μ_{T0}
Equations (6)–(8)	$2.9 \cdot 10^{-5}$	$5.5 \cdot 10^{4}$	$1.7 \cdot 10^{-4}$	$1.3 \cdot 10^{-3}$	$2.7 \cdot 10^{-4}$
'Reference'	$2.9 \cdot 10^{-5}$	$5.5 \cdot 10^{4}$	$1.0 \cdot 10^{-3}$	$1.3 \cdot 10^{-3}$	$1.0 \cdot 10^{-3}$
'High $\eta_\parallel$'	$1.4 \cdot 10^{-4}$	$5.5 \cdot 10^{4}$	$1.0 \cdot 10^{-3}$	$1.3 \cdot 10^{-3}$	$1.0 \cdot 10^{-3}$
'High $\mu_{\Omega 0}$'	$2.9 \cdot 10^{-5}$	$5.5 \cdot 10^{4}$	$1.0 \cdot 10^{-3}$	$8.0 \cdot 10^{-3}$	$1.0 \cdot 10^{-3}$
'Low $\perp$dissipation'	$2.9 \cdot 10^{-5}$	$5.5 \cdot 10^{4}$	$2.5 \cdot 10^{-4}$	$1.3 \cdot 10^{-3}$	$2.5 \cdot 10^{-4}$

to as 'Low $\perp$ dissipation' (as also reported on the third, fourth, and fifth rows of table 2). We note that in the following we enhance particle diffusion, viscosity, and perpendicular electron heat conductivity by a factor 10 in the proximity of the inner and outer radial boundaries to provide buffer regions, which are not included in the analysis of the results.

A first-principles self-consistent model for simulating plasma-neutral interactions in realistic magnetic geometry is not implemented yet in STORM. Therefore, the ionization of neutral atoms near the LCFS and the resulting generation of plasma particles is mimicked with a poloidally and toroidally constant S_n, with a Gaussian profile centered at the LCFS in the radial direction, as shown in figure 1(a). Also the energy source S_E, used to mimic the heat outflowing from the core, is assumed poloidally and toroidally constant, but with a Gaussian profile centered at $\bar{\psi} \approx 0.95$, as illustrated in figure 1(b), with $\bar{\psi} = (\psi - \psi_0)/(\psi_a - \psi_0)$ the normalized poloidal flux, and ψ_0 and ψ_a the poloidal flux at the magnetic axis and at the LCFS, respectively. The amplitudes of S_n and S_E are then adjusted such that the simulated plasma densities and temperatures approximately agree with the experimental measurements at the LCFS.

For the present investigation we consider a radial domain extending in the outer SOL from $\bar{\psi} = 0.9$ to $\bar{\psi} = 1.11$. This corresponds to a distance at the outer mid-plane of approximately 8 cm between the inner and the outer boundaries, x_i and x_o, with 4 cm in the tokamak core and 4 cm in the SOL. We note that, for the discharge considered, the first limiting structure in the SOL was one of the poloidal field coils, located at 5 cm mapped to the mid-plane. Therefore, our domain captures most of the main SOL. On the other hand, in the inner SOL and in the PFRs we expect density and temperature gradients to be steeper than in the outer SOL. Therefore, the inner and outer boundaries are located at $\bar{\psi} = \approx 0.97$ in the PFRs and at $\bar{\psi} \approx 1.04$ in the inner SOL, respectively, as presented in figure 1(c). Ad hoc boundary conditions are then applied at the inner and outer boundaries, as discussed in more detail in appendix A.

We note that, because three-dimensional simulations require rather large numerical grids to resolve plasma turbulence, for the present investigation we simulate only one

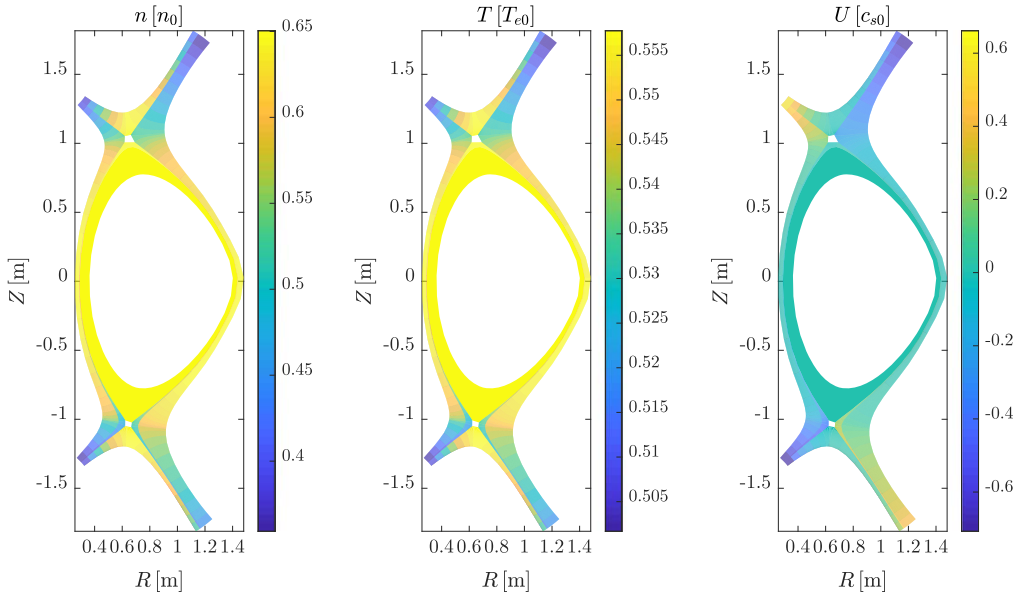

Figure 2. Initial profiles of the plasma density n (left panel), electron temperature T (center panel) and parallel ion velocity U (right panel).

quarter of the torus to decrease the computational cost (i.e. we assume periodicity between $\varphi = 0$ and $\varphi = \pi/2$). This corresponds to neglecting the toroidal mode numbers $n = 1, 2, 3$. We also note that all quantities related to the magnetic equilibrium and to the computation of the grids, necessary as input parameters for STORM simulations, are computed from an EFIT reconstruction of the experimental magnetic field with the grid generator HYPNOTOAD [9]. In the present paper we consider a numerical grid $N_x \times N_y \times N_z$, with $N_x = 276$, $N_y = 96$, and $N_z = 128$ the number of grid points in x, y, and z, respectively. The planes of constant y resulting from such a grid are represented on figure 1(c) as black lines, while the radial grid-spacing and the magnetic separatrices are shown on figure 1(d). We observe that the two separatrices are extremely close, with a gap at the outer mid-plane of only 6 mm. Finally, we note that, while the grid chosen for our simulations ensures a perpendicular resolution at the mid-planes up to $k_\perp \rho_{s0} \simeq 1$, with $\rho_{s0} \approx 2$ mm, near the X-points the radial resolution is coarser due to the natural flux expansion (the radial grid spacing near the X-points increases up to 1 cm). An investigation of the impact of grid-resolution on simulation results is presented in appendix B.

The simulations used in the present paper are initialized from ad hoc axisymmetric profiles, to which we add small amplitude random noise [the initial profiles of n, T, and U are shown in figure 2, while for the other fields we use $V = U$, $\phi = \Lambda T$, and $\Omega = \nabla \cdot (B^{-2} \nabla_\perp \phi)$]. The sources then inject plasma particles and heat, steepening the plasma profiles and triggering plasma-gradient driven instabilities. After an initial transient phase, a statistical steady state is reached (we note that all the fields are fully saturated, except for n, which shows a secular trend, although relatively weak), in which the plasma is eventually removed because of parallel losses at the divertor plates and turbulent radial transport. In the following, we focus our analysis only on this saturated statistical steady state, assuming that, from a statistical point of view, the results do not depend on the initial transient.

5. Comparison between experimental and numerical results at the outer mid-plane

In order to assess the reliability of the STORM model in describing the SOL plasma dynamics, we compare numerical results at the outer mid-plane from the four simulations discussed in section 4 with experimental measurements from the reciprocating Gundestrup probe (note that part of these experimental measurements were also compared with two-dimensional simulations in [33]). For our comparison we consider the following observables: (i) $I_{\rm sat}$ and $V_{\rm fl}$ time-averaged profiles; (ii) statistical properties of $I_{\rm sat}$ and $V_{\rm fl}$ time traces, including the amplitude of the fluctuations, the skewness and the kurtosis of the probability distribution functions (PDFs) as function of the radial position, and the PDFs and power spectral densities (PSDs) at different radial locations; and (iii) statistical properties of intermittent events, including $I_{\rm sat}$ and $V_{\rm fl}$ conditional averaged temporal wave forms, auto-correlation functions of $I_{\rm sat}$ and $V_{\rm fl}$ fluctuations, average times spent by $I_{\rm sat}$ and $V_{\rm fl}$ signals above and below a given threshold, and averaged waiting times between $I_{\rm sat}$ and $V_{\rm fl}$ maxima.

We note that, while the $I_{\rm sat}$ and $V_{\rm fl}$ experimental time traces are obtained from the Gundestrup probe installed on the reciprocating manipulator as explained in section 2, $I_{\rm sat}$ and $V_{\rm fl}$ are not a direct output of STORM. A discussion on how to obtain synthetic $I_{\rm sat}$ and $V_{\rm fl}$ time traces from STORM simulations is presented in appendix C. We also note that, to estimate the statistical uncertainties affecting the simulation results, we proceed as follows. Taking the time-averaged ion saturation current as an example, we evaluate $\langle I_{\rm sat} \rangle_t$ at $\varphi = 0$ and $\varphi = \pi/4$. We then compute $\langle I_{\rm sat} \rangle_t$ as the average of

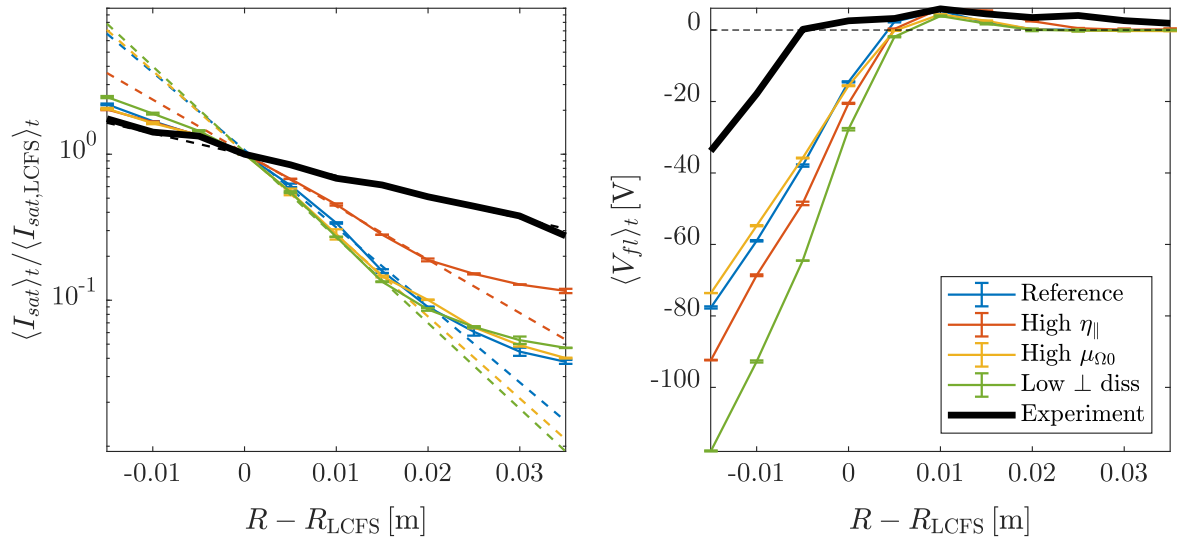

Figure 3. I_{sat} (left panel) and V_{fl} (right panel) time-averaged profiles for the experimental measurements (thick black lines) and the STORM simulations (thin color lines). The $\langle I_{\mathrm{sat}}\rangle_t$ profiles are normalized to their values at the LCFS. The dashed lines in the left panel denote a fit $\langle I_{\mathrm{sat}}\rangle_t(R - R_{\mathrm{LCFS}}) \propto \exp[-(R - R_{\mathrm{LCFS}})/\lambda_{I_{\mathrm{sat}}}]$ between $R - R_{\mathrm{LCFS}} = 0$ cm and $R - R_{\mathrm{LCFS}} = 1.5$ cm. The error bars represent one standard deviation of the results evaluated at $\varphi = 0$ and $\varphi = \pi/4$.

the two resulting values and we take std$[\langle I_{\mathrm{sat}}\rangle_t(\varphi = 0), \langle I_{\mathrm{sat}}\rangle_t(\varphi = \pi/4)]$ as an estimate of the statistical uncertainty affecting $\langle I_{\mathrm{sat}}\rangle_t$, where std denotes the standard deviation. The same procedure is used for all the other observables. In the following subsections we discuss in more detail the evaluation of each observable and the agreement between experimental measurements and simulation results relative to each observable.

5.1. Time-averaged profiles

First, we consider the I_{sat} and V_{fl} time-averaged profiles, $\langle I_{\mathrm{sat}}\rangle_t$ and $\langle V_{\mathrm{fl}}\rangle_t$. These are obtained as the time-average of the 2 ms I_{sat} and V_{fl} sub-signals at each radial position. The results are presented in figure 3. Concerning $\langle I_{\mathrm{sat}}\rangle_t$, the profiles are steeper in the simulations than in the experiment, in particular in the proximity of the LCFS. Furthermore, the perpendicular collisional dissipation parameters seem to play a minor role in setting the gradient of $\langle I_{\mathrm{sat}}\rangle_t$, whereas $\eta_\parallel$ has a stronger impact. This insensitivity of the $\langle I_{\mathrm{sat}}\rangle_t$ profile to changes in the perpendicular collisional dissipation parameters suggests that plasma turbulence is actually the main drive of the perpendicular transport, while collisional diffusion plays a minor role.

To assess more quantitatively the disagreement between the numerical and experimental time-averaged ion saturation current profiles, we fit the results shown in figure 3, left panel, between $R - R_{\mathrm{LCFS}} = 0$ cm and $R - R_{\mathrm{LCFS}} = 1.5$ cm as $\langle I_{\mathrm{sat}}\rangle_t(R - R_{\mathrm{LCFS}}) \propto \exp[-(R - R_{\mathrm{LCFS}})/\lambda_{I_{\mathrm{sat}}}]$. We obtain $\lambda_{I_{\mathrm{sat}}} \simeq 3.0$ cm for the experimental measurements and $\lambda_{I_{\mathrm{sat}}} \simeq 0.8$ cm for the 'reference' simulation. Moreover, we note that an increase of $\mu_{\Omega 0}$ by approximately a factor 6 or a reduction of μ_{n0}, μ_{T0}, μ_{U0}, and μ_{V0} by a factor 4 lead to changes in $\lambda_{I_{\mathrm{sat}}}$ smaller than 10%. On the other hand, an increase of the Spitzer resistivity by approximately a factor 5 leads to a 47% increase of $\lambda_{I_{\mathrm{sat}}}$.

Concerning $\langle V_{\mathrm{fl}}\rangle_t$, we see that the shape of the experimental and numerical profiles are in qualitative agreement, increasing in the core and decreasing in the SOL. We speculate that this is due to simulating both the closed and the open field line regions, since a previous investigation of the RFX-mod SOL plasma dynamics simulating the open field line region only showed qualitative disagreement in $\langle V_{\mathrm{fl}}\rangle_t$ between simulations and experimental measurements [34]. Figure 3 also shows that the experimental profile in the core is radially shifted with respect to the numerical results. We note that neglecting the ion temperature dynamics might play a role in this respect, as V_{fl} depends in general on ϕ, T_e and T_i. Moreover, since the circulation of plasma currents in the SOL potentially determines the position of the bending point of V_{fl} [54], the Boussinesq approximation could also be responsible for this discrepancy. We also note that the collisional dissipation parameters play a noticeable role in setting the gradient of $\langle V_{\mathrm{fl}}\rangle_t$ in the core, which increases by decreasing the perpendicular dissipation parameters or by increasing the plasma resistivity. We also observe that an increase of the Spitzer resistivity leads to a broader $\langle V_{\mathrm{fl}}\rangle_t$ profile in the SOL.

5.2. Statistical properties of I_{sat} and V_{fl} time traces

To gain a deeper insight into the discrepancies in $\langle I_{\mathrm{sat}}\rangle_t$ and $\langle V_{\mathrm{fl}}\rangle_t$ between experimental measurements and numerical results, we also compare the statistics of the fluctuations of the signals. First, in figure 4 we present the amplitude of normalized I_{sat} and V_{fl} fluctuations, $\sigma_{I_{\mathrm{sat}}}/\langle I_{\mathrm{sat}}\rangle_t$ and $\sigma_{V_{\mathrm{fl}}}$, for the experiment and the simulations, where $\sigma_{I_{\mathrm{sat}}}$ and $\sigma_{V_{\mathrm{fl}}}$ are calculated as the standard deviation of the 2 ms sub-signals. The trends in the experiment are well captured by the simulations, with relative I_{sat} fluctuations increasing and V_{fl} fluctuations decreasing as we move radially outwards. These trends are in agreement with observations in most magnetic confinement devices, where large I_{sat} fluctuations are observed in the SOL

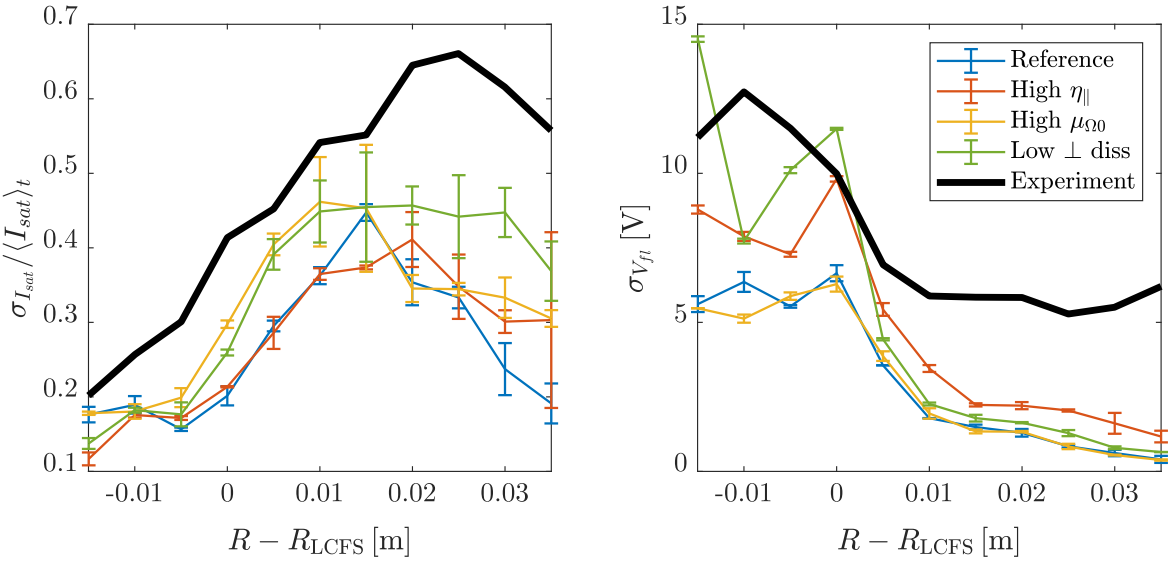

Figure 4. Amplitude of I_{sat} (left panel) and V_{fl} (right panel) fluctuations for the experimental measurements (thick black lines) and the STORM simulations (thin color lines). The I_{sat} fluctuations are normalized to $\langle I_{\mathrm{sat}}\rangle_t$. The error bars represent one standard deviation of the results evaluated at $\varphi = 0$ and $\varphi = \pi/4$.

and are typically associated with the presence of coherent structures, often referred to as plasma filaments (see, e.g. [55]). On the other hand, we note that the decreasing trend of V_{fl} fluctuations was not observed when simulating plasma turbulence in limited configuration in a region with open field lines only [34]. Despite the good qualitative agreement, figure 4 also shows that the simulations underestimate the amplitude of the fluctuations, both for I_{sat} and V_{fl}. This is particularly true in the far SOL and was also observed in previous three-dimensional SOL plasma simulations (see, e.g. [34]).

The third and fourth moments of a PDF are the skewness, S, and the kurtosis, K. The first is a measure of the asymmetry of the PDF, with $S > 0$ indicating a majority of bursts above the average, while the second provides a measure of how likely extreme events are, with $K > 3$ an indicator that the PDF has heavy tails and with a larger number of extreme deviations. We note that a more convenient quantity for comparing the tails of a PDF is the so-called flatness, $F = K - 3$, since $S = F = 0$ for a Gaussian PDF. In the context of plasma physics, $S(I_{\mathrm{sat}}) > 0$ suggests the presence of filaments hotter and denser than the plasma background, whereas $S(I_{\mathrm{sat}}) < 0$ suggests the predominance of plasma holes, which have the opposite behavior. Similarly, $F(I_{\mathrm{sat}}) > 0$ suggests that plasma turbulence is not dominated by small random fluctuations, but rather by extreme coherent events, such as filaments.

The radial profiles of $S(I_{\mathrm{sat}})$, $S(V_{\mathrm{fl}})$, $F(I_{\mathrm{sat}})$ and $F(V_{\mathrm{fl}})$ and the corresponding statistical uncertainties are presented in figures 5 and 6. We observe that $S(I_{\mathrm{sat}}) \approx 0$ at the LCFS, both in the simulations and in the experiment. Moreover, $S(I_{\mathrm{sat}})$ increases moving radially outwards, with $S(I_{\mathrm{sat}}) \gtrsim 1$ in the SOL, in agreement also with previous experimental SOL investigations [56–58]. On the other hand, $S(I_{\mathrm{sat}})$ in the core is larger in the simulations than in the experiment. The impact of dissipation coefficients on $S(I_{\mathrm{sat}})$ is typically smaller than statistical uncertainties. Concerning $S(V_{\mathrm{fl}})$, the experimental profile is almost flat, with $S(V_{\mathrm{fl}}) \approx 0$, and the simulation results generally agree within uncertainties with experimental measurements. Concerning $F(I_{\mathrm{sat}})$ and $F(V_{\mathrm{fl}})$, we observe that simulations and experimental measurements are in quantitative agreement, with $F(I_{\mathrm{sat}}) \approx 0$ at the LCFS and increasing in the SOL, and $F(V_{\mathrm{fl}}) \approx 0$ in the entire domain.

Our observations on the statistical properties of the I_{sat} and V_{fl} time traces are confirmed by comparing the PDFs of I_{sat} and V_{fl} fluctuations, normalized to their standard deviation, at the three radial locations $R - R_{\mathrm{LCFS}} = -1$ cm, $R - R_{\mathrm{LCFS}} = 0$ cm, and $R - R_{\mathrm{LCFS}} = 2$ cm, as shown in figure 7. The simulations accurately capture the well documented transition [20, 59–63] from quasi-Gaussian statistics of I_{sat} at the LCFS to positively skewed in the far SOL. Concerning the collisional dissipation coefficients, we note a remarkable insensitivity of the results, only broken in PDF(V_{fl}) in the core when $\mu_{\Omega 0}$ is increased.

To conclude our investigation of ion saturation current and floating potential fluctuations, in figure 8 we present the PSDs, normalized to $\sigma_{I_{\mathrm{sat}}}$ and $\sigma_{V_{\mathrm{fl}}}$, at the three radial positions $R - R_{\mathrm{LCFS}} = -1$ cm, $R - R_{\mathrm{LCFS}} = 0$ cm, and $R - R_{\mathrm{LCFS}} = 2$ cm. The simulations are in good quantitative agreement with experimental measurements in the far SOL, showing a plateau between $f \approx 4$ kHz and $f \approx 60$ kHz, and then monotonically decreasing for $f > 60$ kHz. This is also in agreement with previous experimental SOL investigations and it is generally associated to the presence of coherent weakly interacting plasma structures [63, 64]. On the other hand, larger differences are observed in the PSDs between simulations and experimental measurements in the core and at the LCFS, with the PSDs almost flat in the simulations for all $f > 4$ kHz, while the experimental measurements monotonically decrease for $f > 30$ kHz. It is worth reminding that in our simulations the source of plasma particles is located at the LCFS. This might have an impact on these results.

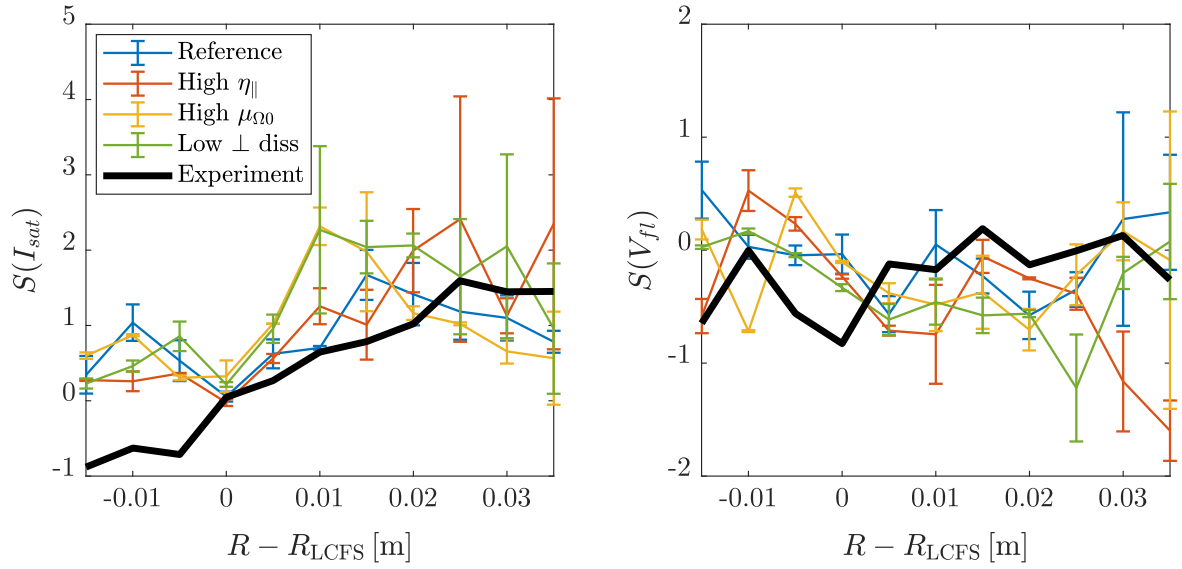

Figure 5. Skewness of the I_{sat} (left panel) and V_{fl} (right panel) PDFs for the experimental measurements (thick black lines) and the STORM simulations (thin color lines). The error bars represent one standard deviation of the results evaluated at $\varphi = 0$ and $\varphi = \pi/4$.

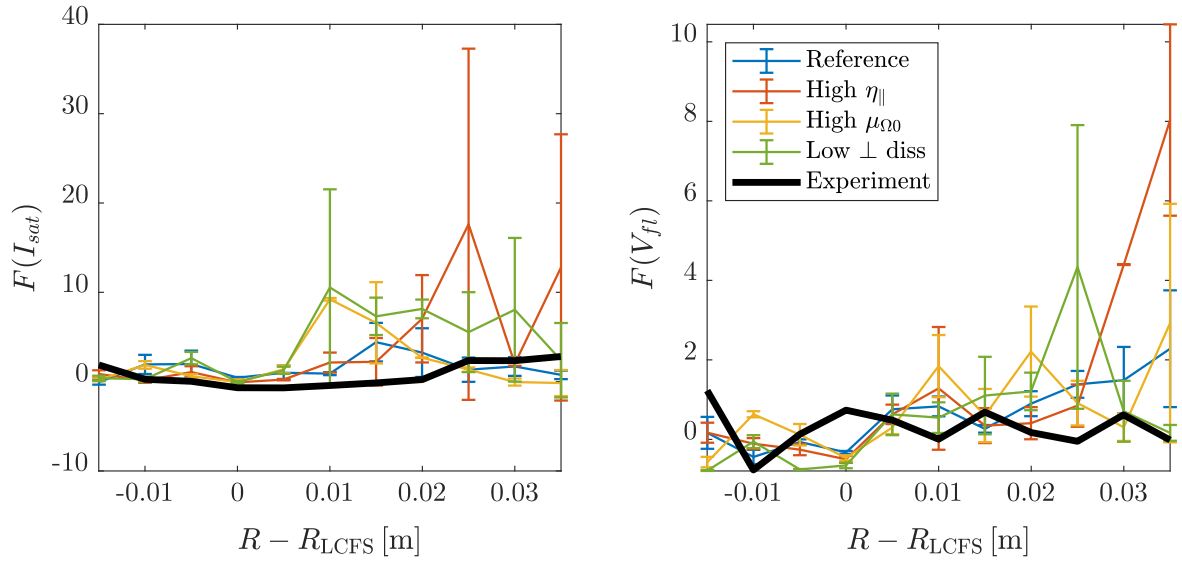

Figure 6. Flatness of the I_{sat} (left panel) and V_{fl} (right panel) PDFs for the experimental measurements (thick black lines) and the STORM simulations (thin color lines). The error bars represent one standard deviation of the results evaluated at $\varphi = 0$ and $\varphi = \pi/4$.

Collisional dissipation parameters do not seem to play a major role in setting the shape of the PSDs.

5.3. Statistical properties of intermittent events

In the tokamak SOL, strongly skewed and intermittent I_{sat} time traces are typically associated with filamentary structures transporting particles and heat towards the main walls of the device. To gain a deeper insight into these structures, we compare some properties of the simulated and experimental bursty events in the I_{sat} and V_{fl} signals, which are typically generated as a plasma filament passes by the position of the probe.

First, we determine the average time evolution of the bursts by calculating the I_{sat} and V_{fl} conditionally averaged temporal wave forms, $C_{\mathrm{avg}}[(I_{\mathrm{sat}} - \langle I_{\mathrm{sat}}\rangle_t)/\sigma_{I_{\mathrm{sat}}}]$ and $C_{\mathrm{avg}}[(V_{fl} - \langle V_{fl}\rangle_t)/\sigma_{V_{fl}}]$, with trigger conditions based on the maximum amplitude of the fluctuations $(I_{\mathrm{sat}} - \langle I_{\mathrm{sat}}\rangle_t)/\sigma_{I_{\mathrm{sat}}} > 2$ and $(V_{\mathrm{fl}} - \langle V_{\mathrm{fl}}\rangle_t)/\sigma_{V_{\mathrm{fl}}} > 2$. While this criterion selects a similar number of experimental and numerical I_{sat} bursts in the SOL (12 in the experiment and 7–10 in the simulations), in the core many fewer events are selected in the experiment than in the simulations (2 in the experiment and 7–12 in the simulations). Moreover, we note that, in general, there are more extreme events in I_{sat} than in V_{fl} time traces, the only exception being the experimental measurements in the core.

The resulting $C_{\mathrm{avg}}[(I_{\mathrm{sat}} - \langle I_{\mathrm{sat}}\rangle_t)/\sigma_{I_{\mathrm{sat}}}]$ and $C_{\mathrm{avg}}[(V_{\mathrm{fl}} - \langle V_{\mathrm{fl}}\rangle_t)/\sigma_{V_{\mathrm{fl}}}]$ and the corresponding statistical uncertainties are presented in figure 9 for the three radial positions $R - R_{\mathrm{LCFS}} = -1$ cm, $R - R_{\mathrm{LCFS}} = 0$ cm, and $R - R_{\mathrm{LCFS}} = 2$ cm. Concerning $C_{\mathrm{avg}}[(I_{\mathrm{sat}} - \langle I_{\mathrm{sat}}\rangle_t)/\sigma_{I_{\mathrm{sat}}}]$, we see good quantitative agreement in the far SOL, both in amplitude and

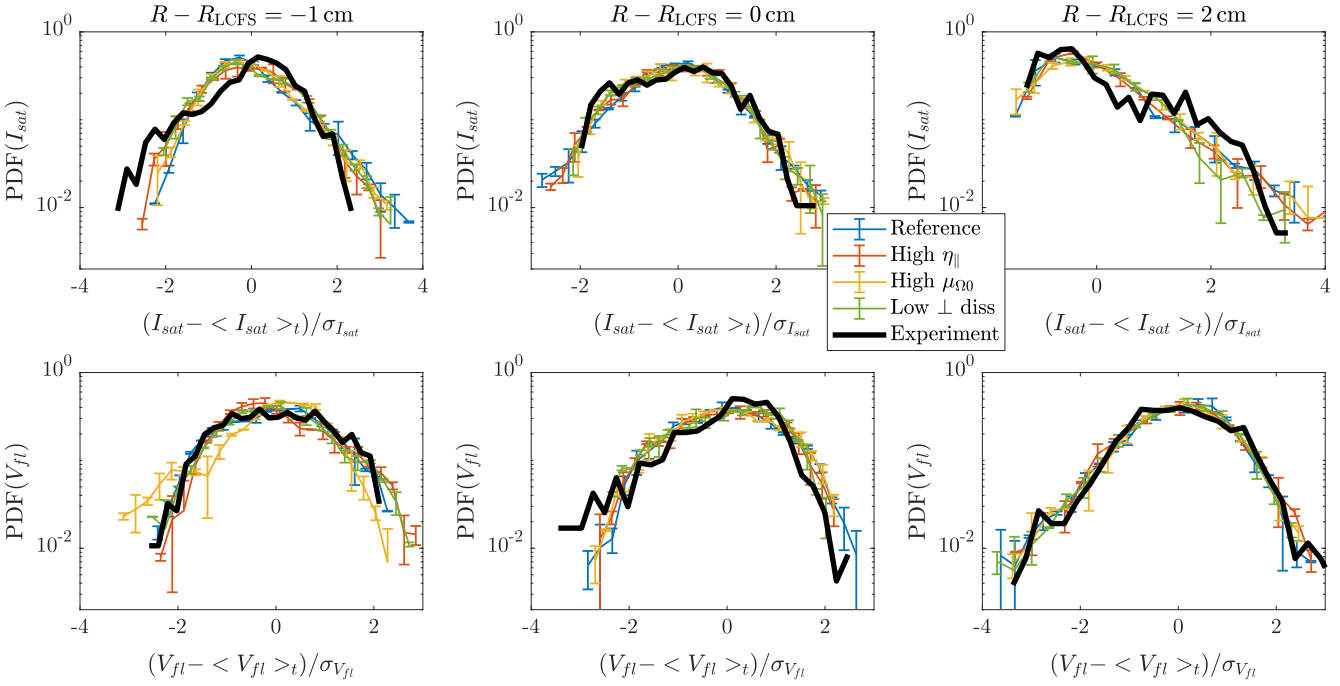

Figure 7. PDFs of $(I_{\mathrm{sat}} - \langle I_{\mathrm{sat}}\rangle_t)/\sigma_{I_{\mathrm{sat}}}$ (first row) and $(V_{\mathrm{fl}} - \langle V_{\mathrm{fl}}\rangle_t)/\sigma_{V_{\mathrm{fl}}}$ (second row) at the three radial locations $R - R_{\mathrm{LCFS}} = -1$ cm (first column), $R - R_{\mathrm{LCFS}} = 0$ cm (second column), and $R - R_{\mathrm{LCFS}} = 2$ cm (third column) for the experimental measurements (thick black lines) and the STORM simulations (thin color lines). The error bars represent one standard deviation of the results evaluated at $\varphi = 0$ and $\varphi = \pi/4$.

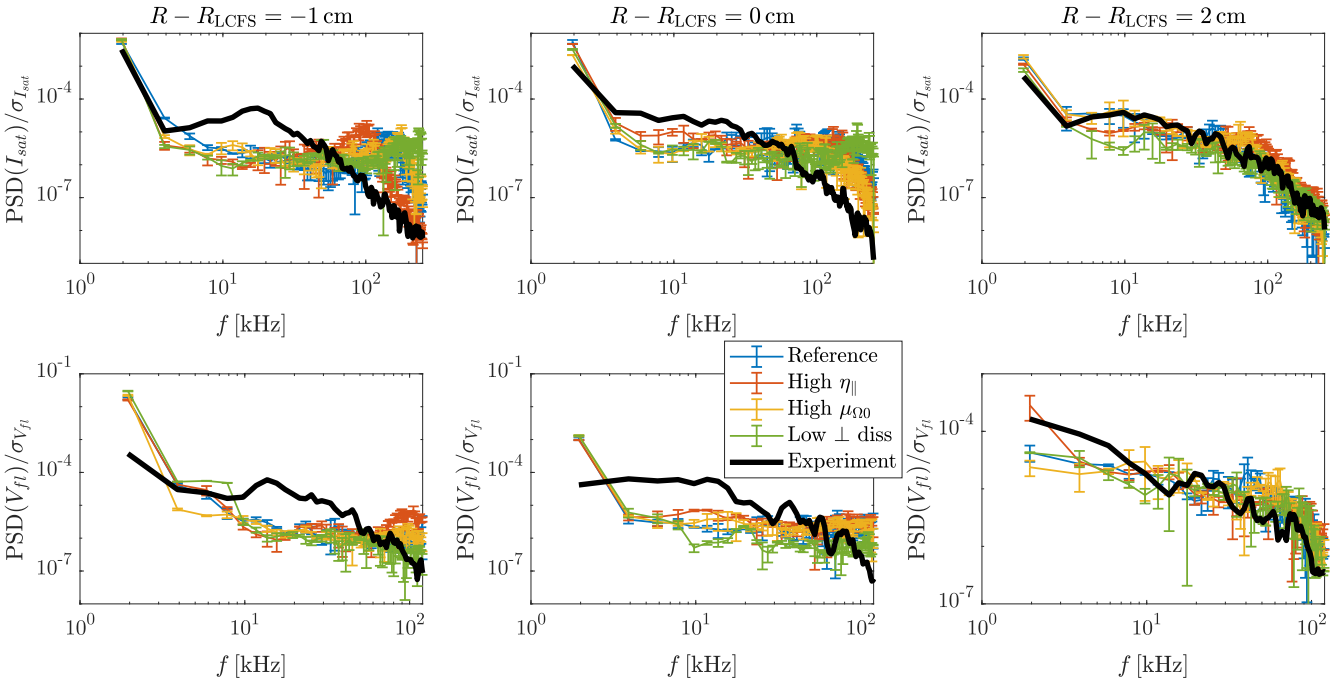

Figure 8. I_{sat} (first row) and V_{fl} (second row) PSDs, normalized to the fluctuation levels, at the three radial locations $R - R_{\mathrm{LCFS}} = -1$ cm (first column), $R - R_{\mathrm{LCFS}} = 0$ cm (second column), and $R - R_{\mathrm{LCFS}} = 2$ cm (third column) for the experimental measurements (thick black lines) and the STORM simulations (thin color lines). The error bars represent one standard deviation of the results evaluated at $\varphi = 0$ and $\varphi = \pi/4$.

width. The shape of $C_{\mathrm{avg}}[(I_{\mathrm{sat}} - \langle I_{\mathrm{sat}}\rangle_t)/\sigma_{I_{\mathrm{sat}}}]$ is quite symmetric, in agreement also with previous analysis of MAST fluctuations [61]. We also observe that collisional dissipation coefficients barely affect the shape of $C_{\mathrm{avg}}[(I_{\mathrm{sat}} - \langle I_{\mathrm{sat}}\rangle_t)/\sigma_{I_{\mathrm{sat}}}]$, but they have a bigger impact on its amplitude. On the other hand, the agreement in $C_{\mathrm{avg}}[(I_{\mathrm{sat}} - \langle I_{\mathrm{sat}}\rangle_t)/\sigma_{I_{\mathrm{sat}}}]$ is worse in the core and at the LCFS, with the conditionally averaged peaks much wider in the experiment than in the simulations.

Concerning $C_{\mathrm{avg}}[(V_{\mathrm{fl}} - \langle V_{\mathrm{fl}}\rangle_t)/\sigma_{V_{\mathrm{fl}}}]$, we observe that in the far SOL the simulation results display a negative peak a

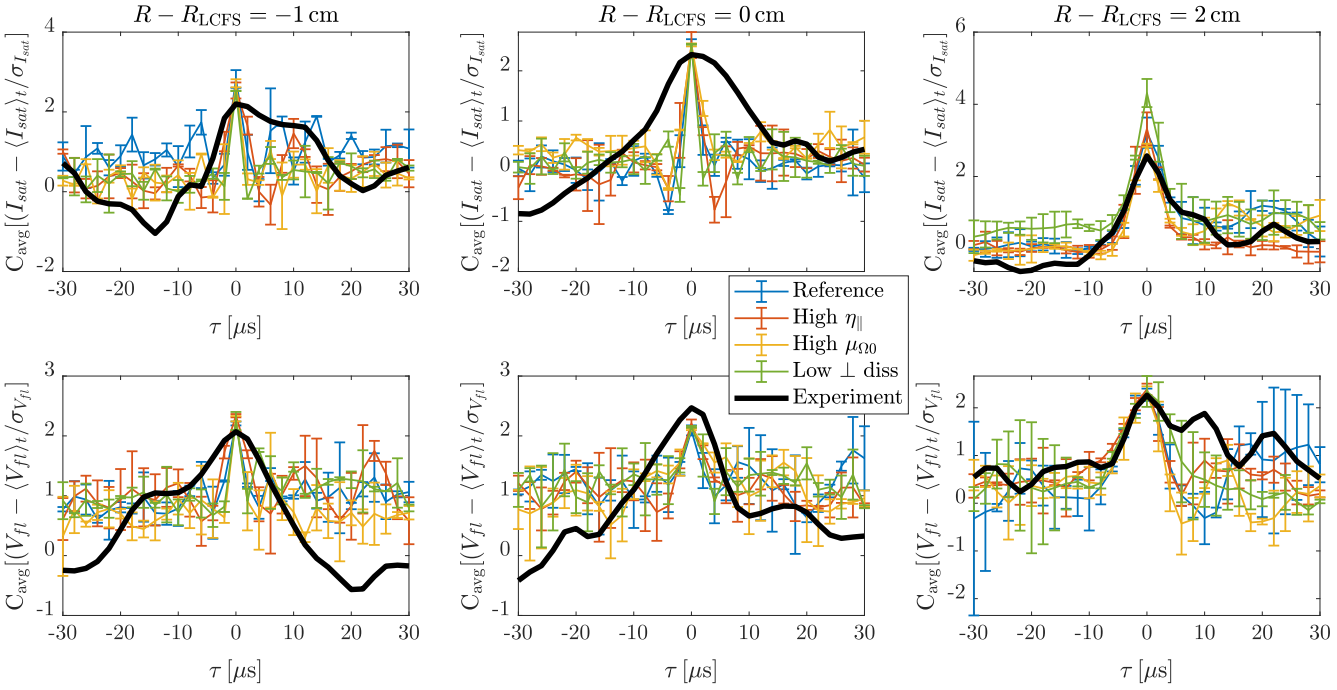

Figure 9. Conditionally averaged temporal wave forms of I_{sat} (first row) and V_{fl} (second row) fluctuations at the three radial locations $R - R_{\mathrm{LCFS}} = -1$ cm (first column), $R - R_{\mathrm{LCFS}} = 0$ cm (second column), and $R - R_{\mathrm{LCFS}} = 2$ cm (third column) for the experimental measurements (thick black lines) and the STORM simulations (thin color lines). The error bars represent one standard deviation of the results evaluated at $\varphi = 0$ and $\varphi = \pi/4$.

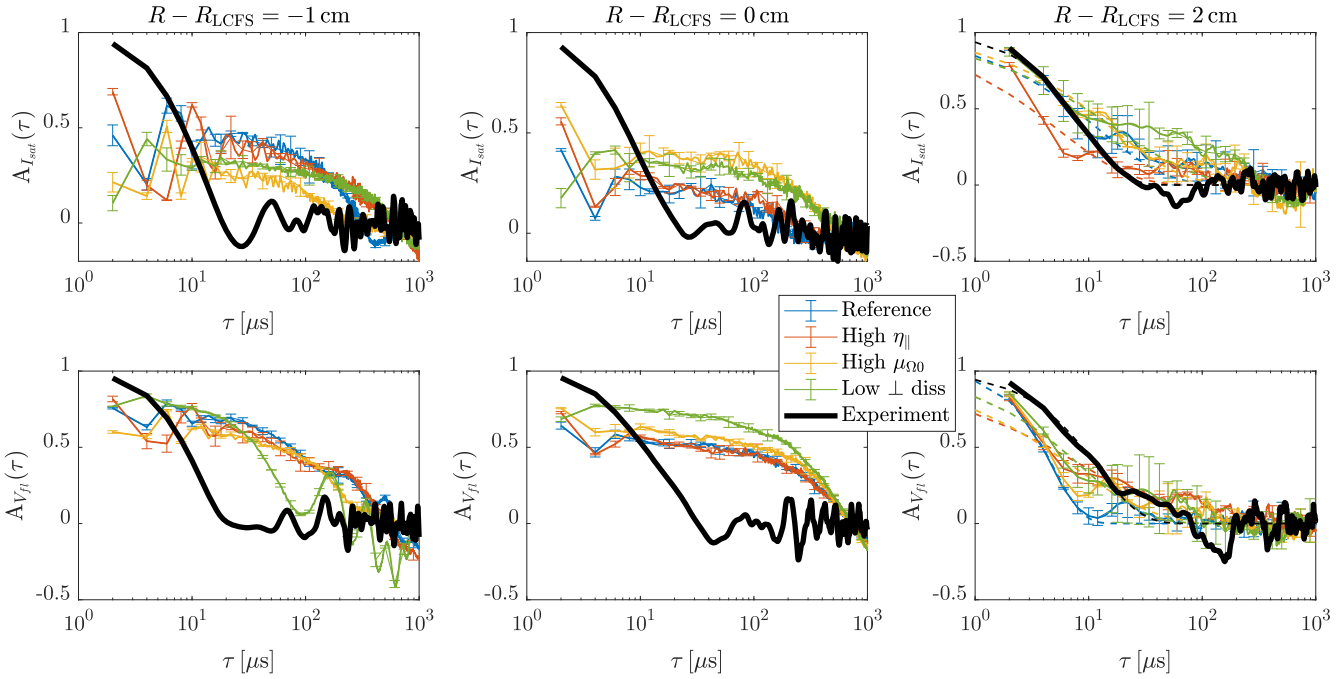

Figure 10. Auto-correlation functions of I_{sat} (first row) and V_{fl} (second row) fluctuations at the three radial locations $R - R_{\mathrm{LCFS}} = -1$ cm (first column), $R - R_{\mathrm{LCFS}} = 0$ cm (second column), and $R - R_{\mathrm{LCFS}} = 2$ cm (third column) for the experimental measurements (thick black lines) and the STORM simulations (thin color lines). The dashed lines denote a fit $A(\tau) = \exp[-(\tau/\tau_c)^{\beta-1}]$ between $\tau = 0$ and $\tau = 20\ \mu$s. The error bars represent one standard deviation of the results evaluated at $\varphi = 0$ and $\varphi = \pi/4$.

few microseconds after the conditional time $\tau = 0$. This suggests the presence of a dipolar structure in V_{fl}. This behavior is not observed in the experimental measurements considered here. However, we note that the literature reports dipolar structures (see, e.g. [65]). Slightly better agreement between simulations and experimental measurements is found in the core and at the LCFS for $C_{\mathrm{avg}}[(V_{\mathrm{fl}} - \langle V_{\mathrm{fl}}\rangle_t)/\sigma_{V_{\mathrm{fl}}}]$ than for $C_{\mathrm{avg}}[(I_{\mathrm{sat}} - \langle I_{\mathrm{sat}}\rangle_t)/\sigma_{I_{\mathrm{sat}}}]$.

Table 3. Auto-correlation times τ_c in experimental measurements and simulation results in the far SOL.

	Experiment	'Reference' simulation	'High $\eta_{\|\|}$' simulation	'High $\mu_{\Omega 0}$' simulation	'Low $\perp$diss' simulation
$\tau_c(I_{sat})$	9 μs	12 μs	5 μs	16 μs	17 μs
$\tau_c(V_{fl})$	12 μs	5 μs	9 μs	8 μs	9 μs

A more quantitative characterization of the temporal time scales in I_{sat} and V_{fl} time traces is provided by computing the auto-correlation function $A(\tau)$ (see, e.g. [33] for its definition). Figure 10 shows $A(\tau)$ for I_{sat} and V_{fl} at the three radial locations discussed above. In general, we observe a better agreement between numerical results and experimental measurements in the far SOL than in the core or at the LCFS. However, we note that the numerical results strongly depend on the collisional dissipation parameters used in the simulations and are affected by quite large statistical uncertainties.

To provide a more quantitative assessment of the agreement between simulations and experiment in the far SOL, we fit the auto-correlation functions between $\tau = 0$ and $\tau = 20\,\mu$s as $A(\tau) = \exp[-(\tau/\tau_c)^{\beta-1}]$, with τ_c the auto-correlation time and β the cascade index. Concerning the auto-correlation times, these are presented in table 3. In the experiment we find $\tau_c \approx 9, 12\,\mu$s for I_{sat} and V_{fl}, respectively. While a similar value is obtained considering the numerical I_{sat} time trace from the 'reference' simulation, a smaller numerical τ_c is found considering V_{fl}. The collisional dissipation coefficients have a quite strong impact on τ_c. Concerning the cascade index, it results that β is typically larger in the experiment ($\beta \approx 2.1$–2.2) than in the simulations ($\beta \approx 1.5$–1.8) and that the collisional dissipation coefficients barely affect it.

Other interesting quantities characterizing intermittent events in I_{sat} and V_{fl} time traces are the relative average time spent above and below a given threshold, $\langle\Delta t\rangle_{above}$ and $\langle\Delta t\rangle_{below}$, and the averaged waiting times between intermittent events, $\langle\tau_w\rangle$. The relative average time spent above (below) a given threshold is computed as the ratio of the total time spent above (below) the threshold to the number of up-crossings (down-crossing) in the 2 ms time intervals. The averaged waiting time for a given threshold between bursts is computed as $\langle\tau_w\rangle = \sum_{j=2}^{N}(t_j - t_{j-1})/N$, where N is the number of up-crossings of the given threshold and t_j are the times at which these events occur. These quantities provide useful information on the duration and separation in time of burst events.

We present $\langle\Delta t\rangle_{above}$ and $\langle\Delta t\rangle_{below}$, normalized to 2 ms, and $\langle\tau_w\rangle$ as function of the selected thresholds in figures 11 and 12. In the experiment, I_{sat} signals spend more time above a given threshold in the SOL than in the core or at the LCFS. This is consistent with the presence of intermittent structures in the SOL. On the other hand, while good agreement between simulations and experimental measurements is found in the SOL both for I_{sat} and V_{fl}, the agreement is worse moving radially inwards.

Similar results are found for $\langle\tau_w\rangle$. Concerning the experimental measurements, we observe that the averaged waiting time for a given threshold decreases moving radially outwards, both for I_{sat} and V_{fl}. On the other hand, while rather good agreement is found between simulations and experimental measurements in the far SOL, larger differences are observed in the core and at the LCFS. Figures 11 and 12 also show that the impact of collisional dissipation parameters on $\langle\Delta t\rangle_{above}$, $\langle\Delta t\rangle_{below}$, and $\langle\tau_w\rangle$ is rather small.

5.4. Discussion

From our investigation of the equilibrium profiles and fluctuation properties it emerges that the major difference between experimental measurements and simulations lies in averaged profiles and the level of fluctuations. This could imply that the radial transport in the experiment is larger than in the simulations in the SOL, which in turn would explain why time-averaged experimental profiles are flatter than the numerical profiles. However, we remark that, as discussed above, an increase of the Spitzer resistivity by approximately a factor 5 leads to flatter profiles (with an increase of approximately 50% in $\lambda_{I_{sat}}$), but has a negligible impact on I_{sat} fluctuations. To investigate if this flattening is related to an increase of the radial velocity of the filaments, in the simulations we also evaluated the level of the fluctuations of the poloidal electric field, σ_{E_θ} (not presented here). This analysis shows that an increase of the Spitzer resistivity by approximately a factor 5 has a negligible impact on σ_{E_θ}. While this study is not conclusive, since a more accurate estimate of the filament velocities would be required (as done, e.g. in [66, 67]), it might suggest that the $\langle I_{sat}\rangle_t$ profiles are steeper in the simulations than in the experiment because of higher parallel losses. Three possible reasons for this discrepancy are (i) the boundary conditions applied at the target plates; (ii) neglecting plasma-neutral interactions, which would slow down plasma particles because of plasma-neutral collisions, in particular near the target plates (see, e.g. [68, 69]); and (iii) the Boussinesq approximation adopted in this work (a preliminary investigation carried out using STORM simulations without the Boussinesq approximation displays noticeably smaller electron parallel velocities near the separatrixes at the target plates). We also note that a previous investigation of the #21712 plasma discharge with a two-dimensional model resulted in better quantitative agreement of the I_{sat} time-averaged profile at the outer mid-plane [33].

The comparison between experimental measurements and simulation results reveals that, even if there is disagreement in I_{sat} and V_{fl} averaged profiles and level of fluctuations, the statistics of plasma turbulence and intermittent events are quite similar in the SOL. We note that SOL plasma fluctuations exhibit several statistical properties which appear universal across devices, plasma parameters and confinement

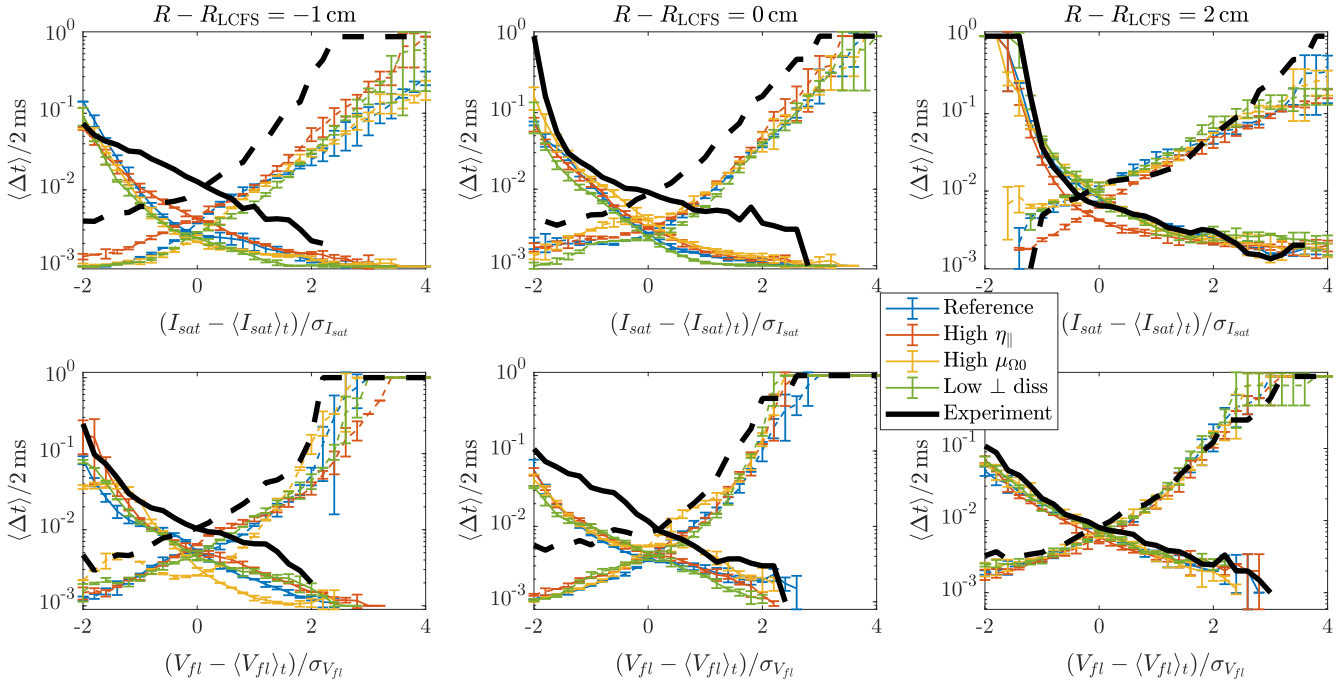

Figure 11. Relative average time spent by I_{sat} (first row) and V_{fl} (second row) fluctuations above (solid lines) and below (dashed lines) a given threshold at the three radial locations $R - R_{\mathrm{LCFS}} = -1$ cm (first column), $R - R_{\mathrm{LCFS}} = 0$ cm (second column), and $R - R_{\mathrm{LCFS}} = 2$ cm (third column) for the experimental measurements (thick black lines) and the STORM simulations (thin color lines). The error bars represent one standard deviation of the results evaluated at $\varphi = 0$ and $\varphi = \pi/4$.

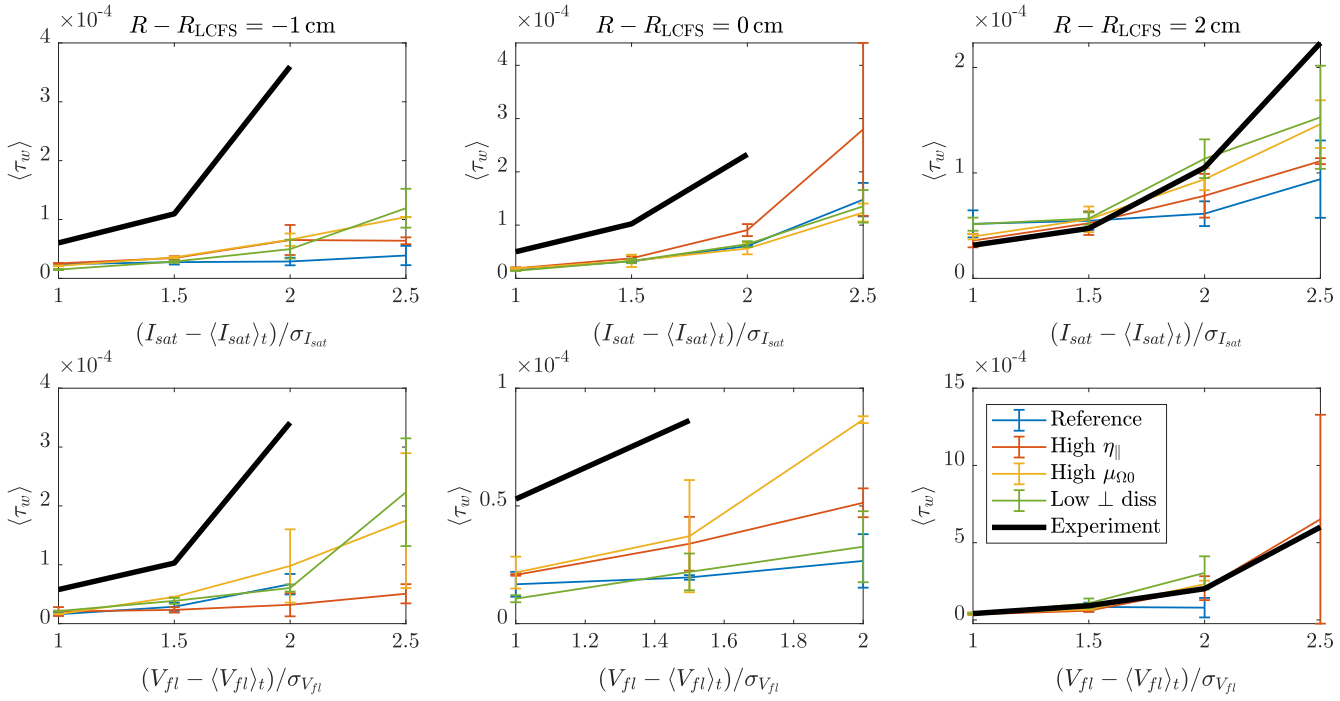

Figure 12. Averaged waiting times between I_{sat} (first row) and V_{fl} (second row) maxima at the three radial locations $R - R_{\mathrm{LCFS}} = -1$ cm (first column), $R - R_{\mathrm{LCFS}} = 0$ cm (second column), and $R - R_{\mathrm{LCFS}} = 2$ cm (third column) for the experimental measurements (thick black lines) and the STORM simulations (thin color lines). The error bars represent one standard deviation of the results evaluated at $\varphi = 0$ and $\varphi = \pi/4$.

modes. In particular, the I_{sat} PDFs are found to be positively skewed and flattened, and to have an exponential tail towards positive values in the SOL (see, e.g. [20, 59–63]). Moreover, the fluctuations show a remarkable similarity across devices also in the frequency domain [61, 63, 64]. Our simulations are able to accurately capture this universal behavior. Nevertheless, we note that MAST represents an exception for what concerns conditionally averaged wave forms of I_{sat} signals. In

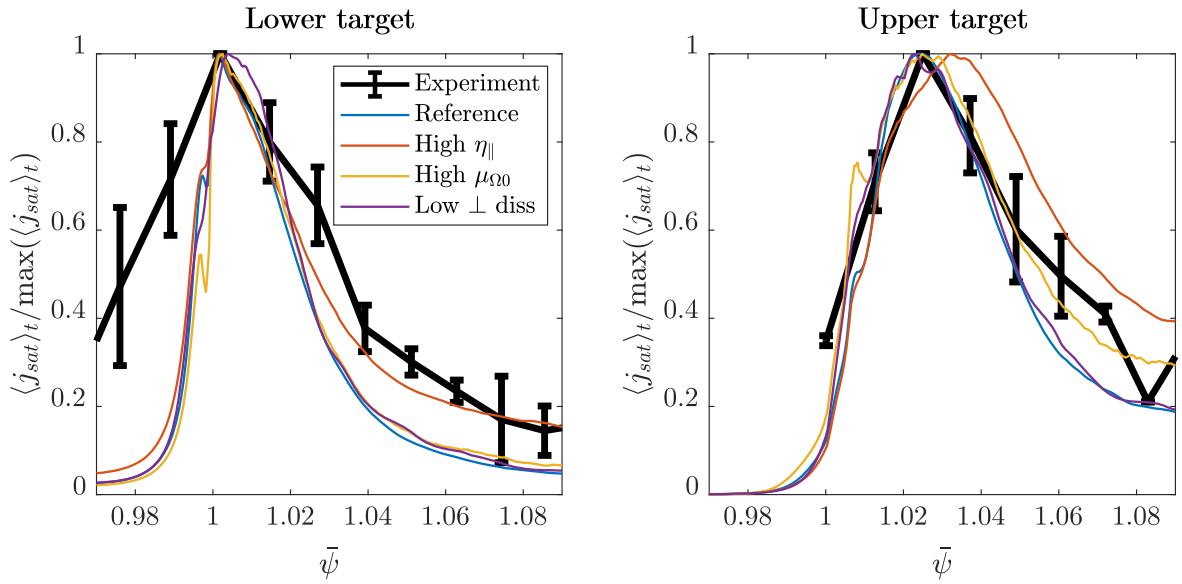

Figure 13. Time-average profiles of j_{sat} normalized to their maximum value at the lower (left panel) and upper (right panel) outer targets from MAST experimental measurements (thick black lines) and STORM simulations (thin color lines). The error bars represent one standard deviation in the experimental data. The experimental profiles are shifted in $\bar{\psi}$ to match the location of the peaks with the simulation results.

fact, while the average shape of the intermittent fluctuations typically appears to be sharply peaked with a faster rise than decay [20, 61, 70], in MAST it is much more symmetric [33]. We also note that the agreement in the fluctuation properties is worse in the core and at the LCFS than in the SOL. However, this might be related to the position of S_n, which is located at the LCFS, and also to the fact that the STORM model is designed to reproduce SOL rather than core physics.

To conclude our discussion, we note that in our simulations we assume cold ions. However, this is a quite strong assumption, since in typical SOL conditions we observe $T_i/T_e \gtrsim 1$ [71–74]. An assessment of the impact of hot ions in MAST was carried out in [30], where it was found that the qualitative behavior of three-dimensional seeded filament simulations with and without T_i effects was similar. We defer the detailed analysis of the impact of ion temperature effects on SOL turbulence in MAST to a future study.

6. Comparison between experimental and numerical results at the outer target plates

Three-dimensional simulations allow a comparison between experimental measurements and numerical results not only at the outer mid-plane, but also at the divertor plates. In figure 13 we present the $\langle j_{\mathrm{sat}}\rangle_t$ radial profiles, normalized to their maximum value, at the lower and upper outer target plates, both for the experimental measurements and the four simulations discussed above (note that the statistical uncertainties affecting numerical results are extremely small and are not displayed here). We recall that the experimental profiles are shifted in $\bar{\psi}$ to match the location of $\langle j_{\mathrm{sat}}\rangle_t$ peaks with the simulation results.

Figure 13 shows that simulations and experimental measurements are in quite good agreement at the upper divertor target. On the other hand, in the lower divertor leg the differences between the experimental and the numerical profiles are larger. This is particularly true in the PFR, where the numerical profiles are much steeper than the experimental measurements. Concerning the differences among the simulation results, we see that the parallel resistivity plays an important role in setting the radial transport in the SOL in the outer divertor legs. In fact, an increase of the Spitzer resistivity by a factor 5 leads to noticeably flatter profiles at the target plates. On the other hand, the perpendicular collisional parameters seem to play a smaller role, suggesting that the transport is governed by turbulence rather than collisions.

We note that in this section we compare the shape of ion saturation current density time-averaged profiles rather than their amplitude. As a matter of fact, neglecting the dynamics of neutral particles in our simulations, in particular the neutral recycling, makes comparing the amplitudes impractical from a quantitative point of view, although the good qualitative agreement found between the shapes suggests that the transport physics is correct. In the experimental measurements at the target plates, $\langle j_{\mathrm{sat}}\rangle_t$ is approximately 5 times larger than in the simulations.

7. Conclusions

In the present paper, global flux-driven STORM simulations based on the MAST L-mode plasma discharge #21712 in double null configuration are discussed. The three-dimensional plasma profiles are evolved self-consistently, with no separation between equilibrium and fluctuations. Energy and plasma particles are injected in the system in the core and at

the LCFS, steepening the plasma profiles and triggering plasma-gradient driven instabilities. After an initial transient phase, the parallel losses at the divertor plates and the turbulent radial transport eventually balance the energy and particle sources, thus reaching a statistical steady state. This represents a major step in the development of STORM, which is now able to simulate plasma turbulence at the edge of tokamak devices such as MAST in realistic diverted configurations.

The simulations are then compared with experimental measurements from a reciprocating Gundestrup probe at the outer mid-plane and from flush-mounted LPs at the divertor plates and the differences observed are investigated. This is the first time that a thorough comparison between experimental measurements and three-dimensional simulations in double null configuration is attempted. The time-averaged profiles are steeper at the outer mid-plane in the simulations than in the experiment, resulting in an ion saturation current decay length approximately 4 times smaller in the numerical results than in the experimental measurements. Additionally, the level of the fluctuations is smaller in the simulations than in the experiment. On the other hand, the STORM model well captures several statistical properties of plasma turbulence and intermittent events in the tokamak SOL, such as the positively skewed ion saturation current PDFs universally observed in magnetic confinement fusion devices, the shape and duration of the bursts in the time traces, and the time-separation between them. The simulation results also qualitatively agree with experimental measurements at the divertor plates. This is a remarkable result, since it means that STORM simulations are a suitable tool for investigating the turbulent plasma transport over the whole poloidal extension of the SOL, including the divertor legs and the PFRs. This was not possible with two-dimensional models. It is also observed that an increase in the parallel plasma resistivity typically leads to flatter profiles, both at the outer mid-plane and at the divertor plates, while other collisional dissipation parameters play a minor role in setting the SOL plasma dynamics.

In general, even if some quantitative discrepancies are observed between numerical results and experimental measurements, in the SOL our simulations are able to qualitatively reproduce all the observables considered in our comparison. We expect that the inclusion of hot ions and plasma-neutral interactions might improve this agreement, but such an investigation is left for future work.

Acknowledgments

The authors gratefully acknowledge helpful discussions with P Ricci and P Tamain. This work has been funded by the RCUK Energy Programme [Grant Number EP/P012450/1]. The simulations presented herein were carried out in part on the CINECA Marconi supercomputer within the framework of the SOL_BOUT project and in part using Archer computing resources under Plasma HEC consortium grants EP/L000237/1 and EP/R029148/1. This work was in part supported by the UK EPSRC funded Collaborative Computational Project in Plasma Physics [grant number EP/M022463/1]. To obtain further information on the data and models underlying this paper please contact PublicationsManager@ukaea.uk.

Appendix A. Boundary conditions

Since the drift approximation breaks down at the magnetic pre-sheath entrance, equations (9)–(10) are used as boundary conditions in y for U, V, and $q_{\parallel}$ at the four divertor plates. On the other hand, to prevent over-constraining the system, a free boundary condition is set in y on the remaining variables (i.e. ϕ, Ω, n, and T are extrapolated in y from the inner domain to the divertor plates with a one-sided third-order finite difference scheme). Additionally, a twist-shift boundary condition is applied in the core to ensure continuity of the field values and periodicity is assumed in the z direction between $z = 0$ and $z = \pi/2$, as discussed in sections 3 and 4.

Since a set of first-principle boundary conditions describing the plasma interaction with the outer wall is not available in the literature, and STORM is not coupled yet with a kinetic model for the tokamak core, ad hoc boundary conditions are applied at the inner and outer boundaries x_i and x_o. More precisely, at x_i and x_o we impose $\langle \partial_x f \rangle_z = 0$ and $\partial_z f = 0$, with $f = n$, Ω, U, V, T and $\langle - \rangle_z$ denoting toroidal averaging. Moreover, we set $\phi(x = x_i) = \langle \phi(x = x_i + \Delta x_i/2) \rangle_{z,t\in[(j-1)\tau, j\tau]}$ and $\phi(x = x_o) = \langle \phi(x = x_o - \Delta x_o/2) \rangle_{z,t\in[(j-1)\tau, j\tau]}$ for all $t \in [j\tau, (j+1)\tau]$, where $j = 1, 2, \ldots, \infty$, τ is an input parameter (in our simulations we use $\tau = 100/\Omega_{i0}$ at x_i and $\tau = 2/\Omega_{i0}$ at x_o), and $\langle - \rangle_{z,t\in[(j-1)\tau, j\tau]}$ denotes a toroidal- and time-average over the time interval $[(j-1)\tau, j\tau]$. To mitigate the impact of these boundary conditions on the simulation results, the two regions extending from $\bar{\psi} = 0.9$ to $\bar{\psi} = 0.95$ and from $\bar{\psi} = 1.09$ to $\bar{\psi} = 1.11$ are considered as buffers and are not included in the analysis of the results.

Appendix B. Scan in grid resolution

To investigate the impact of the grid resolution on the results presented in sections 5 and 6, we performed two additional simulations, one with a resolution $N_x = 184$, $N_y = 72$, and $N_z = 64$, referred in the following as 'coarse'; and one with a resolution $N_x = 404$, $N_y = 136$, and $N_z = 256$, referred in the following as 'refined'. We note that for the 'refined' simulation we considered one third of the torus (i.e. we assume periodicity between $\varphi = 0$ and $\varphi = 2\pi/3$, which corresponds to neglecting the toroidal mode numbers $n = 1, 2$) and, because of the increased computational cost of such a simulation, we have only 1.3 ms of statistics in statistical steady state.

For both simulations we performed the analysis presented in sections 5 and 6 and we compared the results with the 'reference' simulation. We note that from this comparison emerges that the differences between the three simulations in I_{sat} and V_{fl} fluctuation levels, skewness, and flatness are negligible. On the other hand, larger differences are observed

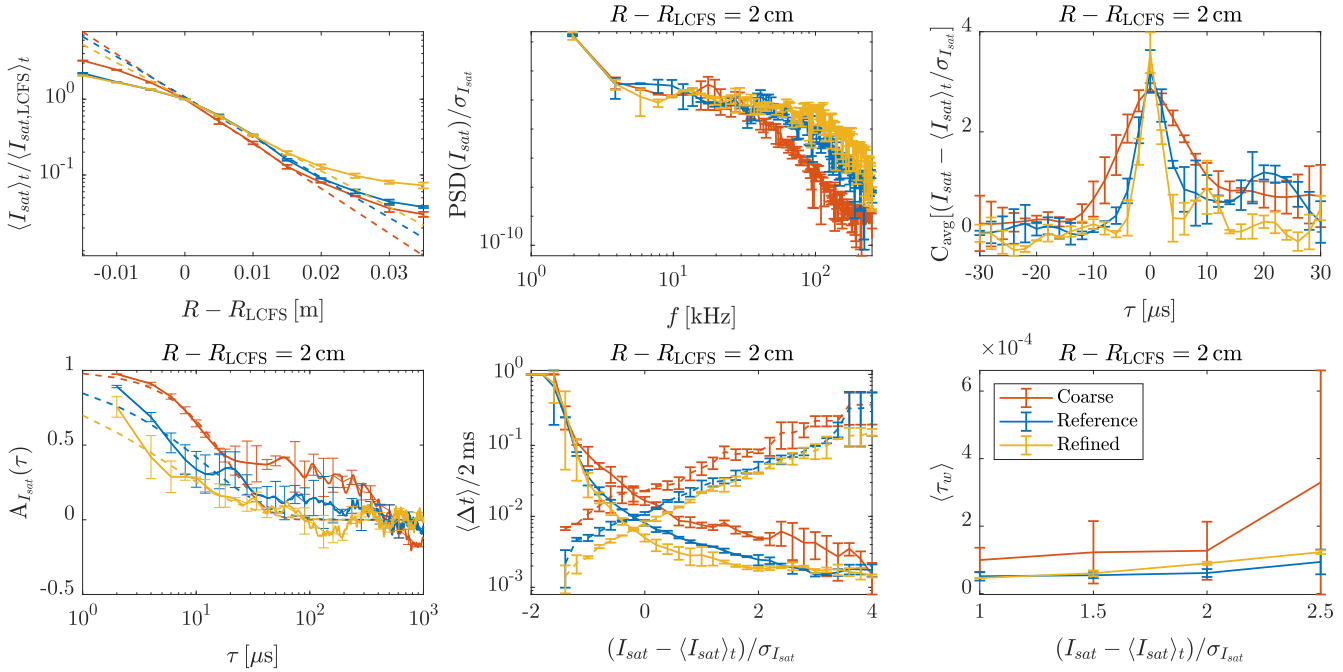

Figure B1. Numerical results at the outer mid-plane for the 'coarse', 'reference', and 'refined' simulations. First row: I_{sat} time-averaged profiles (left panel), PSDs (central panel), and conditional averaged temporal wave forms (right panel). Second row: auto-correlation function of I_{sat} fluctuations (left panel), relative average time spent by I_{sat} signals above (solid lines) and below (dashed lines) a given threshold (central panel), and averaged waiting times between I_{sat} maxima (right panel). The dashed lines in the left panel in the first row denote a fit $\langle I_{\mathrm{sat}}\rangle_t(R - R_{\mathrm{LCFS}}) \propto \exp[-(R - R_{\mathrm{LCFS}})/\lambda_{I_{\mathrm{sat}}}]$ between $R - R_{\mathrm{LCFS}} = 0$ cm and $R - R_{\mathrm{LCFS}} = 1.5$ cm and the ones in the second row denote a fit $A(\tau) = \exp[-(\tau/\tau_c)^{\beta-1}]$ between $\tau = 0$ and $\tau = 20\,\mu$s. The error bars represent one standard deviation of the results evaluated at $\varphi = 0$ and $\varphi = \pi/4$.

in the other quantities. The most relevant ones are shown in figure B1.

Concerning the I_{sat} averaged profiles at the outer mid-plane (figure B1 first row, left panel), an increase in the resolution leads to flatter profiles, with approximately a 30% increase of $\lambda_{I_{\mathrm{sat}}}$ between the 'coarse' and the 'refined' simulation. An increase in the resolution also leads to flatter PSDs and thinner I_{sat} conditional averaged temporal wave forms (figure B1 first row, central and right panels). We note that similar results (not shown here) are obtained for the PSDs and the conditional averaged temporal wave forms of V_{fl}. Concerning the auto-correlation times, an increase in resolution results in shorter correlation times, from $\tau_c \approx 20\,\mu$s for the 'coarse' simulation to $\tau_c \approx 12\,\mu$s and $\tau_c \approx 6\,\mu$s for the 'reference' and 'refined' simulations, respectively (figure B1 second row, left panel). On the other hand, the cascade index is barely affected by changing the resolution, with $\beta \approx 1.4$–1.6 for all simulations. The largest differences in the relative average time spent by I_{sat} time traces above and below a given threshold are observed between the 'coarse' and the 'reference' simulation, while the changes between the 'reference' and the 'refined' simulation are much smaller (figure B1 second row, central panel). Similar conclusions are obtained for the averaged waiting times between I_{sat} maxima (figure B1 second row, right panel).

In general, it results that the observables obtained with the 'reference' and the 'refined' simulations are extremely close. The only exceptions are the averaged profiles and the conditional averaged temporal wave forms However, these differences are typically smaller than the differences between numerical results and experimental measurements, suggesting that our considerations in sections 5–7 do not depend on the grid resolution considered for our analysis.

To gain a deeper insight into the impact of grid resolution on turbulence properties, in figure B2 we show the electron pressure, $p = nT$, and electrostatic potential, ϕ, wavenumber spectra, normalized to the fluctuation levels, in the far SOL for the 'coarse', 'reference', and 'refined' simulations. We observe that the spectra are similar at low poloidal wavenumbers, k_θ, whereas the bending point between the energy cascade and dissipation regimes is shifted toward higher k_θ at higher resolutions. We also see that the wavenumber spectrum for the reference and the refined simulations agree up to $k_\theta \rho_{s0} \simeq 0.5$. Since the drift approximation breaks down for $k_\perp \rho_{s0} \gtrsim 1$, the grid resolution considered in sections 5 and 6 is appropriate for our investigation.

Appendix C. Synthetic diagnostics

The numerical I_{sat} and V_{fl} time traces used to compute the observables discussed in sections 5 and 6 are obtained by post-processing the simulation results with a synthetic reciprocating probe at the outer mid-plane and synthetic LPs at the target plates. More precisely, we assume $I_{\mathrm{sat}} \propto n\sqrt{T}$ and $V_{fl} = T/e - 2.83\phi$, where n, T, and ϕ are obtained from

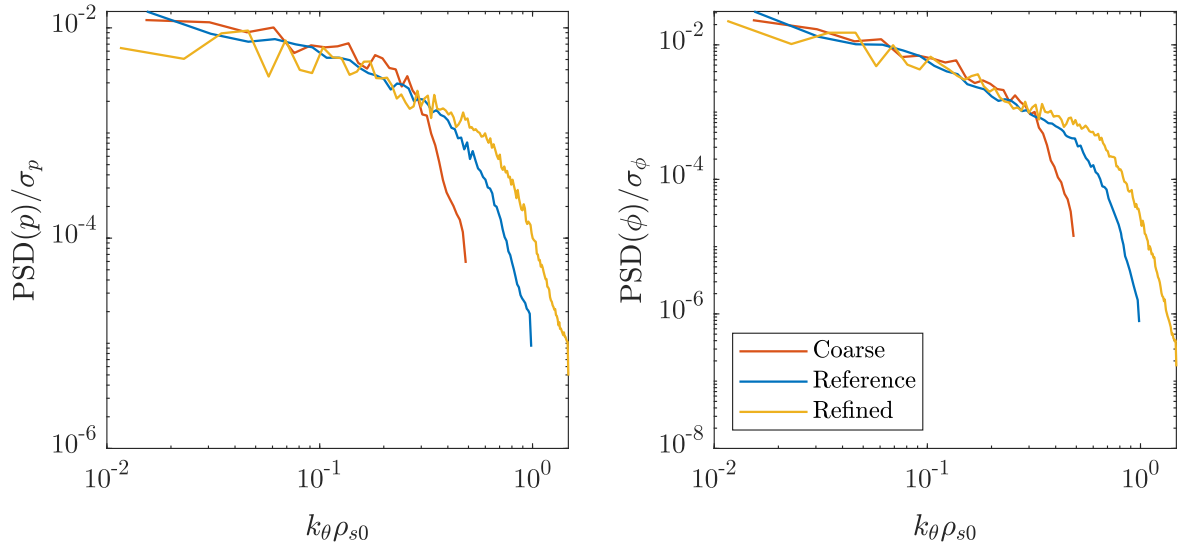

Figure B2. Electron pressure $p = nT$ (left panel) and electrostatic potential ϕ (right panel) wavenumber spectra, normalized to the fluctuation levels, at the radial location $R - R_{\mathrm{LCFS}} = 2$ cm for the 'coarse' (red lines), 'reference' (blue lines), and 'refined' (yellow lines) simulations.

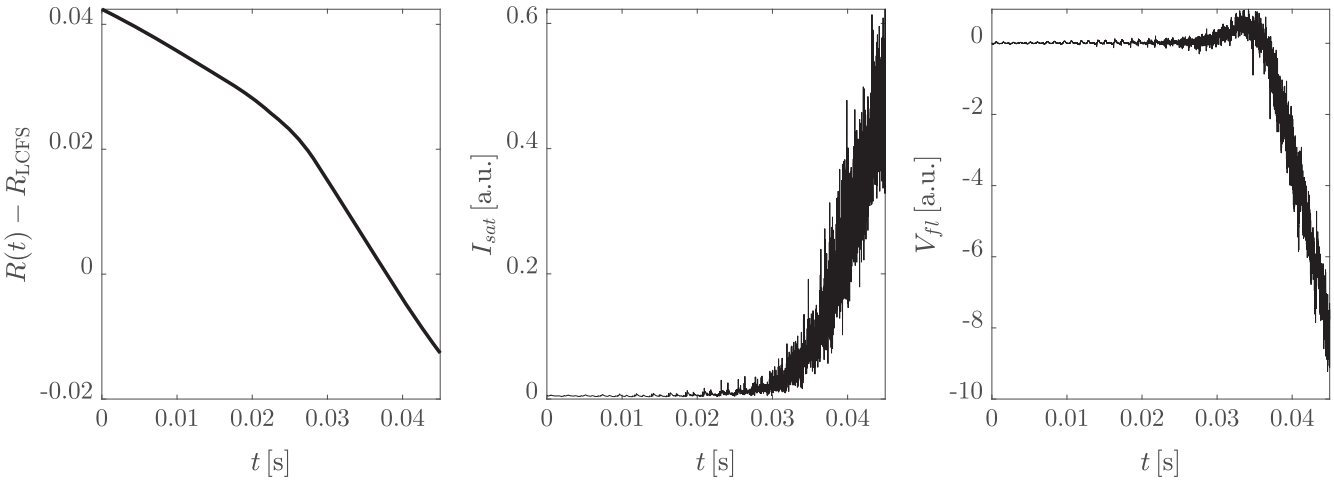

Figure C1. Distance of the synthetic reciprocating probe from the LCFS (left panel) and synthetic time traces of ion saturation current (center panel) and floating potential (right panel) in arbitrary units.

STORM simulations with plasma quantities in statistical steady state (except for n, which shows a secular trend, although relatively weak) on time intervals of approximately 2 ms. The profiles discussed in section 6 are then obtained by time and toroidally averaging the resulting time traces at the divertor plates. On the other hand, for the synthetic reciprocating probe we proceed as follows. First, at each radial position at the outer mid-plane we concatenate several copies of the numerical I_{sat} and V_{fl} time traces to obtain signals of approximately 0.05 s. Second, we produce a synthetic time trace $R(t)$, where R is the distance of the synthetic probe from the axis of symmetry of the tokamak, emulating the radial movement of the reciprocating manipulator entering the plasma, as shown in figure C1, left panel. Third, we identify all the times t_j, with $0 \leqslant t_j \leqslant 0.05$ s, at which $R(t)$ is half way in between grid points. Finally, we concatenate the time traces of I_{sat} and V_{fl} on the different time intervals $[t_0, t_1]$, $[t_1, t_2]$, …, where for each sub-interval $[t_j, t_{j+1}]$ we evaluate I_{sat} and V_{fl} on the grid point closest to $R((t_j + t_{j+1})/2)$. Examples of the resulting synthetic time traces are given in figure C1, center and right panels.

This procedure allows us to obtain the observables shown in section 5 by processing experimental measurements and synthetic time traces with exactly the same methodology. We note that, to investigate if these results depend on the approach used to post-process STORM simulations, we performed an additional analysis (not shown here), where we considered I_{sat} and V_{fl} synthetic time traces at fixed positions at the outer mid-plane on time intervals of approximately 2 ms. It results that differences in the observables obtained with the two approaches are typically smaller than the statistical uncertainties and that the discussion in section 5 is not affected by the methodology used to post-process the numerical results.

ORCID iDs

Fabio Riva https://orcid.org/0000-0002-0264-442X
Fulvio Militello https://orcid.org/0000-0002-8034-4756
John T Omotani https://orcid.org/0000-0002-3156-8227
Ben Dudson https://orcid.org/0000-0002-0094-4867
Nick R Walkden https://orcid.org/0000-0002-0661-5909

References

[1] Loarte A *et al* (the ITPA Scrape-off Layer and Divertor Physics Topical Group) 2007 Power and particle control *Nucl. Fusion* **47** S203–63
[2] Zohm H *et al* 2013 On the physics guidelines for a tokamak DEMO *Nucl. Fusion* **53** 073019
[3] Ricci P 2015 Simulation of the scrape-off layer region of tokamak devices *J. Plasma Phys.* **81** 435810202
[4] Fasoli A, Brunner S, Cooper W A, Graves J P, Ricci P, Sauter O and Villard L 2016 Computational challenges in magnetic-confinement fusion physics *Nat. Phys.* **12** 411–23
[5] Dudson B D and Leddy J 2017 Hermes: global plasma edge fluid turbulence simulations *Plasma Phys. Control. Fusion* **59** 054010
[6] Easy L, Militello F, Omotani J, Dudson B, Havlíčková E, Tamain P, Naulin V and Nielsen A H 2014 Three dimensional simulations of plasma filaments in the scrape off layer: a comparison with models of reduced dimensionality *Phys. Plasmas* **21** 122515
[7] Walkden N R, Easy L, Militello F and Omotani J T 2016 Dynamics of 3D isolated thermal filaments *Plasma Phys. Control. Fusion* **58** 115010
[8] Dudson B D, Umansky M V, Xu X Q, Snyder P B and Wilson H R 2009 BOUT++: a framework for parallel plasma fluid simulations *Comput. Phys. Commun.* **180** 1467–80
[9] Dudson B D *et al* 2015 BOUT++: Recent and current developments *J. Plasma Phys.* **81** 365810104
[10] Garcia O E, Naulin V, Nielsen A H and Rasmussen J J 2004 Computations of intermittent transport in scrape-off layer plasmas *Phys. Rev. Lett.* **92** 165003
[11] Garcia O E, Bian N H, Naulin V, Nielsen A H and Rasmussen J J 2005 Mechanism and scaling for convection of isolated structures in nonuniformly magnetized plasmas *Phys. Plasmas* **12** 090701
[12] Nielsen A, Xu G, Madsen J, Naulin V, Juul Rasmussen J and Wan B 2015 Simulation of transition dynamics to high confinement in fusion plasmas *Phys. Lett.* A **379** 3097–101
[13] Ricci P, Halpern F D, Jolliet S, Loizu J, Mosetto A, Fasoli A, Furno I and Theiler C 2012 Simulation of plasma turbulence in scrape-off layer conditions: the GBS code, simulation results and code validation *Plasma Phys. Control. Fusion* **54** 124047
[14] Halpern F D, Ricci P, Jolliet S, Loizu J, Morales J, Mosetto A, Musil F, Riva F, Tran T M and Wersal C 2016 The GBS code for tokamak scrape-off layer simulations *J. Comput. Phys.* **315** 388–408
[15] Zhu B, Francisquez M and Rogers B N 2018 GDB: a global 3D two-fluid model of plasma turbulence and transport in the tokamak edge *Comput. Phys. Commun.* **232** 46–58
[16] Stegmeir A, Coster D, Ross A, Maj O, Lackner K and Poli E 2018 GRILLIX: a 3D turbulence code based on the flux-coordinate independent approach *Plasma Phys. Control. Fusion* **60** 035005
[17] Tamain P, Bufferand H, Ciraolo G, Colin C, Galassi D, Ghendrih P, Schwander F and Serre E 2016 The TOKAM3X code for edge turbulence fluid simulations of tokamak plasmas in versatile magnetic geometries *J. Comput. Phys.* **321** 606–23
[18] Braginskii S I 1965 Transport processes in a plasma *Rev. Plasma Phys.* **1** 205
[19] Simakov A N and Catto P J 2004 Drift-ordered fluid equations for modelling collisional edge plasma *Contrib. Plasma Phys.* **44** 83–94
[20] Garcia O, Horacek J, Pitts R, Nielsen A, Fundamenski W, Naulin V and Rasmussen J J 2007 Fluctuations and transport in the TCV scrape-off layer *Nucl. Fusion* **47** 667–76
[21] Halpern F D, Ricci P, Jolliet S, Loizu J and Mosetto A 2014 Theory of the scrape-off layer width in inner-wall limited tokamak plasmas *Nucl. Fusion* **54** 043003
[22] Riva F, Lanti E, Jolliet S and Ricci P 2017 Plasma shaping effects on tokamak scrape-off layer turbulence *Plasma Phys. Control. Fusion* **59** 035001
[23] Walkden N, Riva F, Dudson B, Ham C, Militello F, Moulton D, Nicholas T and Omotani J 2019 3D simulations of turbulent mixing in a simplified slab-divertor geometry *Nucl. Mater. Energy* **18** 111–7
[24] Oberkampf W L and Trucano T G 2002 Verification and validation in computational fluid dynamics *Prog. Aerosp. Sci.* **38** 209–72
[25] Oberkampf W L and Roy C J 2010 *Verification and Validation in Scientific Computing* (New York, NY: Cambridge University Press)
[26] Roache P J 1998 *Verification and Validation in Computational Science and Engineering* (Albuquerque, NM: Hermosa Publishers)
[27] Riva F, Ricci P, Halpern F D, Jolliet S, Loizu J and Mosetto A 2014 Verification methodology for plasma simulations and application to a scrape-off layer turbulence code *Phys. Plasmas* **21** 062301
[28] Dudson B D, Madsen J, Omotani J, Hill P, Easy L and Løiten M 2016 Verification of BOUT++ by the method of manufactured solutions *Phys. Plasmas* **23** 062303
[29] Riva F *et al* 2016 Blob dynamics in the TORPEX experiment: a multi-code validation *Plasma Phys. Control. Fusion* **58** 044005
[30] Militello F *et al* 2016 Multi-code analysis of scrape-off layer filament dynamics in MAST *Plasma Phys. Control. Fusion* **58** 105002
[31] Ricci P, Riva F, Theiler C, Fasoli A, Furno I, Halpern F D and Loizu J 2015 Approaching the investigation of plasma turbulence through a rigorous verification and validation procedure: a practical example *Phys. Plasmas* **22** 055704
[32] Garcia O E, Horacek J, Pitts R A, Nielsen A H, Fundamenski W, Graves J P, Naulin V and Rasmussen J J 2006 Interchange turbulence in the TCV scrape-off layer *Plasma Phys. Control. Fusion* **48** L1–10
[33] Militello F, Tamain P, Fundamenski W, Kirk A, Naulin V and Nielsen A H 2013 Experimental and numerical characterization of the turbulence in the scrape-off layer of MAST *Plasma Phys. Control. Fusion* **55** 025005
[34] Riva F, Vianello N, Spolaore M, Ricci P, Cavazzana R, Marrelli L and Spagnolo S 2018 Three-dimensional simulations of plasma turbulence in the RFX-mod scrape-off layer and comparison with experimental measurements *Phys. Plasmas* **25** 022305
[35] Omotani J T, Militello F, Easy L and Walkden N R 2016 The effects of shape and amplitude on the velocity of scrape-off layer filaments *Plasma Phys. Control. Fusion* **58** 014030
[36] Easy L, Militello F, Omotani J, Walkden N R and Dudson B 2016 Investigation of the effect of resistivity on scrape off layer filaments using three-dimensional simulations *Phys. Plasmas* **23** 012512

[37] Militello F, Dudson B, Easy L, Kirk A and Naylor P 2017 On the interaction of scrape off layer filaments *Plasma Phys. Control. Fusion* **59** 125013

[38] Yang Y, Counsell G and (the MAST Team) 2003 Observations with a mid-plane reciprocating probe in MAST *J. Nucl. Mater.* **313–316** 734–7

[39] MacLatchy C S, Boucher C, Poirier D A and Gunn J 1992 Gundestrup: a Langmuir/Mach probe array for measuring flows in the scrape-off layer of TdeV *Rev. Sci. Instrum.* **63** 3923–9

[40] Kirk A, Ahn J-W and Counsell G 2003 The influence of the divertor magnetic configuration and of ELM frequency on target heat fluxes in MAST *J. Nucl. Mater.* **313–316** 1081–4

[41] Tamain P, Kirk A, Nardon E, Dudson B and Hnat B 2010 Edge turbulence and flows in the presence of resonant magnetic perturbations on MAST *Plasma Phys. Control. Fusion* **52** 075017

[42] Lao L, John H S, Stambaugh R D, Kellman A G and Pfeiffer W 1985 Reconstruction of current profile parameters and plasma shapes in tokamaks *Nucl. Fusion* **25** 1611

[43] Tsui C K *et al* 2017 Poloidal asymmetry in the narrow heat flux feature in the TCV scrape-off layer *Phys. Plasmas* **24** 062508

[44] Russell D A, D'Ippolito D A and Myra J R 2012 On relaxing the Boussinesq approximation in scrape-off layer turbulence (SOLT) model simulations *Bulletin of the American Physical Society, 54th Annual Meeting of the APS Division of Plasma Physics* Vol 57 *(Providence, Rhode Island, USA)* BP8.159

[45] Yu G Q, Krasheninnikov S I and Guzdar P N 2006 Two-dimensional modelling of blob dynamics in tokamak edge plasmas *Phys. Plasmas* **13** 042508

[46] Bodi K, Ciraolo G, Ghendrih P, Schwander F, Serre E and Tamain P 2011 Impact of the Boussinesq approximation in tokamak scrape–off layer turbulence *38th EPS Conf. on Plasma Physics (Strasbourg, France)* P1.121

[47] Ross A, Stegmeir A and Coster D 2018 Effect of the Boussinesq approximation: turbulence studies with GRILLIX in slab geometry *Contrib. Plasma Phys.* **58** 478–83

[48] Stangeby P 2000 *The Plasma Boundary of Magnetic Fusion Devices* (*Series in Plasma Physics and Fluid Dynamics*) (London: Taylor and Francis)

[49] Xu X Q, Umansky M V, Dudson B and Snyder P B 2014 Boundary plasma turbulence simulations for tokamaks *Commun. Comput. Phys.* **4** 949–79

[50] Dimits A M 1993 Fluid simulations of tokamak turbulence in quasiballooning coordinates *Phys. Rev.* E **48** 4070–9

[51] Arakawa A 1966 Computational design for long-term numerical integration of the equations of fluid motion: two-dimensional incompressible flow: I *J. Comput. Phys.* **1** 119–43

[52] Thomas L H 1949 *Elliptic Problems in Linear Differential Equations over a Network* Watson Science Computer Laboratory Report Columbia University: New York, NY

[53] Hindmarsh A C, Brown P N, Grant K E, Lee S L, Serban R, Shumaker D E and Woodward C S 2005 SUNDIALS: suite of nonlinear and differential/algebraic equation solvers *ACM Trans. Math. Softw.* **31** 363–96

[54] Loizu J, Morales J A, Halpern F D, Ricci P and Paruta P 2017 Scrape-off-layer current loops and floating potential in limited tokamak plasmas *J. Plasma Phys.* **83** 575830601

[55] D'Ippolito D A, Myra J R and Zweben S J 2011 Convective transport by intermittent blob-filaments: comparison of theory and experiment *Phys. Plasmas* **18** 060501

[56] Sánchez E *et al* 2000 Statistical characterization of fluctuation wave forms in the boundary region of fusion and nonfusion plasmas *Phys. Plasmas* **7** 1408–16

[57] Xu Y H, Jachmich S, Weynants R R and (the TEXTOR team) 2005 On the properties of turbulence intermittency in the boundary of the TEXTOR tokamak *Plasma Phys. Control. Fusion* **47** 1841–55

[58] Nanobashvili I, Gunn J and Devynck P 2007 Radial profiles of plasma turbulent fluctuations in the scrape-off layer of the Tore Supra tokamak *J. Nucl. Mater.* **363–365** 622–7

[59] Garcia O E, Pitts R A, Horacek J, Madsen J, Naulin V, Nielsen A H and Rasmussen J J 2007 Collisionality dependent transport in TCV SOL plasmas *Plasma Phys. Control. Fusion* **49** B47–57

[60] Antar G Y, Devynck P, Garbet X and Luckhardt S C 2001 Turbulence intermittency and burst properties in tokamak scrape-off layer *Phys. Plasmas* **8** 1612–24

[61] Antar G Y 2004 Universality of intermittent convective transport in the scrape-off layer of magnetically confined devices *Contrib. Plasma Phys.* **44** 217–21

[62] Graves J P, Horacek J, Pitts R A and Hopcraft K I 2005 Self-similar density turbulence in the TCV tokamak scrape-off layer *Plasma Phys. Control. Fusion* **47** L1–9

[63] Garcia O E, Kube R, Theodorsen A, LaBombard B and Terry J L 2018 Intermittent fluctuations in the Alcator C-Mod scrape-off layer for ohmic and high confinement mode plasmas *Phys. Plasmas* **25** 056103

[64] Pedrosa M A *et al* 1999 Empirical similarity of frequency spectra of the edge-plasma fluctuations in toroidal magnetic-confinement systems *Phys. Rev. Lett.* **82** 3621–4

[65] Theodorsen A, Garcia O E, Horacek J, Kube R and Pitts R A 2016 Scrape-off layer turbulence in TCV: evidence in support of stochastic modelling *Plasma Phys. Control. Fusion* **58** 044006

[66] Nespoli F, Furno I, Labit B, Ricci P, Avino F, Halpern F D, Musil F and Riva F 2017 Blob properties in full-turbulence simulations of the TCV scrape-off layer *Plasma Phys. Control. Fusion* **59** 055009

[67] Paruta P, Beadle C, Ricci P and Theiler C 2019 Blob velocity scaling in diverted tokamaks: a comparison between theory and simulation *Phys. Plasmas* **26** 032302

[68] Rensink M E, Lodestro L, Porter G D, Rognlien T D and Coster D P 1998 A comparison of neutral gas models for divertor plasmas *Contrib. Plasma Phys.* **38** 325–30

[69] Kotov V and Reiter D 2009 Two-point analysis of the numerical modelling of detached divertor plasmas *Plasma Phys. Control. Fusion* **51** 115002

[70] Boedo J A *et al* 2001 Transport by intermittent convection in the boundary of the DIII-D tokamak *Phys. Plasmas* **8** 4826–33

[71] Kočan M *et al* 2011 Measurements of ion energies in the tokamak plasma boundary *J. Nucl. Mater.* **415** S1133–8

[72] Tamain P, Kočan M, Gunn J, Kirk A, Pascal J-Y and Price M 2011 Ion energy measurements in the scrape-off layer of MAST using a Retarding Field Analyzer *J. Nucl. Mater.* **415** S1139–42

[73] Elmore S, Allan S Y, Kirk A, Fishpool G, Harrison J, Tamain P, Kočan M, Gaffka R, Stephen R and Bradley J W 2012 Upstream and divertor ion temperature measurements on MAST by retarding field energy analyser *Plasma Phys. Control. Fusion* **54** 065001

[74] Allan S Y, Elmore S, Fishpool G and Dudson B 2016 Ion temperature measurements of L-mode filaments in MAST by retarding field energy analyser *Plasma Phys. Control. Fusion* **58** 045014